FLOW AROUND A SOLITARY TREE IN A LARGE FIELD UNDER NEUTRAL ATMOSPHERIC STRATIFICATION

by

Wyatt J. Horne

A thesis submitted to the faculty of
The University of Utah
in partial fulfillment of the requirements for the degree of

Master of Science

Department of Mechanical Engineering

The University of Utah

December 2012

The University of Utah Graduate School

STATEMENT OF THESIS APPROVAL

The thesis of **Wyatt J. Horne**

has been approved by the following supervisory committee members:

James R. Stoll II	, Chair	**10/01/2012** Date Approved
Eric R. Pardyjak	, Member	**09/19/2012** Date Approved
Meredith M. Metzger	, Member	**09/27/2012** Date Approved

and by **Timothy Ameel** , Chair of the Department of **Mechanical Engineering**

and by Charles A. Wight, Dean of The Graduate School.

ABSTRACT

A large-eddy simulation study was conducted to characterize the bulk momentum and turbulence features of flow around an isolated deciduous tree in the atmospheric boundary layer under neutral stratification. In addition to characterizing the flow field, a simplified model that contained the essential features of flow around an isolated tree was constructed. The flow structure around the tree consisted of a region of high velocity defect and high turbulent kinetic energy behind the tree with accelerated flow around the edges. The region of high velocity defect was found to form near the location of maximum leaf area density of the tree and to then spread and dissipate downstream approximately following a power law. The region of heightened turbulent kinetic energy was found to be dominated by the streamwise velocity variance. The turbulent stresses around the tree were found to have peaks near the edges of the tree with similar structure to axisymmetric and plane wakes. The similarities between the tree wake flow and canonical axisymmetric wakes was used to motivate a simplified empirical model. To agree with the LES data, the empirical model had two important differences to a standard axisymmetric wake model. First, the plume spread was found to be nonsymmetric between the vertical and horizontal directions and therefore, an angular plume dependence was introduced. Second, the isolated tree wake was found to dissipate within a shorter downstream distance than a standard axisymmetric wake model. To address this second difference, the empirical model breaks the wake up into two regions: a near wake region where plume statistics evolve linearly with downstream distance and a far wake region that exhibits power-law behavior. The model was found to accurately reproduce the turbulent stresses, turbulent kinetic energy, and mean velocity for deciduous trees. When tested for sensitivity to the location of maximum leaf area density, the model was found to overpredict the turbulent kinetic energy and streamwise velocity defect at lower locations.

CONTENTS

LIST OF FIGURES

LIST OF TABLES

ACKNOWLEDGMENTS

Computing time on the Center for High Performance Computing and numerous contributions from Rob Stoll are sincerely acknowledged with gratitude. Help received from my very supportive family is also greatly appreciated.

CHAPTER 1

INTRODUCTION

The transport of momentum, thermal energy, water vapor and particulate matter in the atmospheric boundary layer (ABL) are strongly influenced by the presence of plant life. Conversely, the ABL affects the growth of plants; through the impact of turbulence, the long-range dispersion of seeds and pollen, and through wind induced plant damage that can influence habitat and food availability. An accurate description of these ABL-plant life interactions requires the characterization of fluid flow within and around plants [33, 10].

Many studies have examined the influence of plant life on ABL dynamics. Dense plant life such as forests and agricultural crops has been a primary focus of these studies [51, 12, 28, 36]. In these cases, two main flow features have been identified. The first is Kelvin-Helmholtz-like structures that dominate transport processes. The Kelvin-Helmholtz structures are typically ascribed to the development of a mixing layer between the slower canopy fluid flow and the quicker free flow above. This description allows for ready analogy to mixing-layer flows to explain canopy flow features [33, 14]. The second major feature of dense canopy flows is a short-cutting within the turbulent energy cascade. This feature is attributed to small-scale canopy element vortex shedding [8, 29].

The mixing-layer analogy has been found to be inadequate to explain all features of dense canopy flows. In particular, the wavelength of instabilities under the mixing-layer analogy is predicted to scale with mixing layer thickness [19]. In measurements, and in analysis that incorporates the flexibility of the canopy, it has been found that the wavelength of instabilities does not scale with mixing layer thickness over a specific range of velocities for highly flexible canopies [32]. It has also been found that the natural frequency of the plants plays a significant role in the wavelength and frequency of the coherent structures within a dense, highly flexible canopy [32, 10]. This feature cannot be explained using the mixing-layer analogy.

In addition to dense canopies, a strong interest in sparser canopy cases such as wind-breaks, perennial crops and forest clearings exists [52, 22, 21, 27]. In such cases the inflection

point in the streamwise velocity profile, which is essential to the mixing-layer canopy analogy, can be altered significantly [14]. Several experimental and numerical studies have concluded that the mixing-layer analogy fails when the canopy density falls below a critical threshold [12, 25, 20]. One explanation proposed for this is that the flow field becomes dominated by the underlying rough wall boundary layer washing out the mixing layer [20]. A second explanation given is that the spacing between plants becomes increasingly important as the canopy density decreases [25]. This explanation was reinforced by a study conducted on sparse, row-oriented canopies. In this study it was found that as the canopy becomes increasingly sparse, velocity moments do not scale with overall canopy density, but as functions of row density and spacing [3].

An important limiting case of sparse canopies is windbreak flow. In the case of windbreaks, the flow structure transitions from its upstream characteristics into two distinct regions at the windbreak. Along the length of the windbreak, the flow is significantly slower than upstream due to the aerodynamic drag from the windbreak. At the top of the windbreak, the flow experiences a significant acceleration due to streamline displacement. The quicker flow at the top of the windbreak and the slower flow mix downstream of the windbreak until the flow returns to its upstream characteristics [22]. Pressure has been found to play a vital role in the development of these different regions [48]. The interaction between flow and pressure has been attributed to control the location of lowest flow velocity, streamline curvature, extent of flow speed-up at the windbreak top, and the distance it takes the flow to recover to its upstream state [48, 46, 47, 42].

In the extreme case when the canopy is sufficiently sparse, the flow field becomes the superposition of individual plant wakes. Some cases where this can occur are within savanna woodlands, thinned forests, orchards, and urban environments [14]. Such cases are quite commonly encountered in the ABL. For instance, savannas cover roughly an eighth of the global land surface and contain a large portion of the human population. Savannas also contain a majority of the world's rangelands and livestock [35]. Urban environments contain a majority of the human population and are predicted to contain the majority of population growth through 2050 [11]. In order to create an accurate description of cases at this level of extreme sparsity, the flow around individual plants must be characterized.

The research interest in flow around individual plants has been relatively tepid compared to study of dense canopies and the previously discussed sparse canopy cases. In studies of flow around individual plants, a region of high velocity defect is found behind the plant with its center corresponding to a zero crossing of the transverse Reynolds stress [2]. This region

is three-dimensional (3D) in nature and has been found to be strongly influenced by the geometry of the plant [18]. Little research effort has been put forth towards the creation of a model capable of recreating the 3D fluid characteristics of the wake. Such a model would be desirable for use within large scale studies, such as many urban studies, where computational overhead restricts the modeler from rigorously modeling fluid flow around individual plant life.

While the impact of isolated plant life on the fluid flow in the atmosphere has received very little study, the impact of fluid flow on isolated plant life has received significant attention [24, 10, 23, 7]. The focus of many of these studies is the accurate description of the deformation of the tree due to wind forcing. It has been found that in order to properly predict important phenomena such as direct wind induced plant damage the deformation of plant life must be addressed [23].

Large-eddy simulation (LES) has proven to be a powerful tool in the study of canopy flows [36, 52, 20, 12, 50, 40]. LES holds advantages over experiment and other modeling techniques such as Reynolds-averaged Navier-Stokes (RANS) based numerical techniques in that it provides 3D high resolution spatial flow fields as well as resolved temporal flow information including extremes. LES also has the added advantage of control over atmospheric conditions. Most past LES studies of plant canopies have been of homogeneous canopies with a few notable exceptions [52, 5].

In past homogeneous studies the canopy is imposed on the flow field as a forcing term that is dependent on an a priori determined drag coefficient and a leaf area index [36]. The drag coefficient is typically assumed to be spatially uniform and the leaf area density a function of only height. These assumptions have been addressed in more recent LES studies of heterogeneous canopies. One adaption is to partially resolve the spatial structure of the plant-life while accounting for stems and leaves separately. This has been found to have a nontrivial impact on turbulence statistics within a corn canopy when compared to homogeneous results and measured data [52].

The purpose of the present study is to explore the effects of isolated trees on the bulk momentum and turbulence characteristics of flow in the ABL. Of particular interest is the velocity field, turbulent stresses, and variances within the wake region of an isolated tree. Another goal of this study is to create a simplified model that can be used to recreate the primary features of such flows. The selected flow case is flow around a single deciduous tree in a large, grassy field as might be encountered in a savanna or severely thinned forest. In order to acquire the necessary 3D spatial information and resolved temporal information

for the study, LES is used. The simulations are used to find qualitative and quantitative insight on the characteristics of the flow case under neutral atmospheric conditions.

CHAPTER 2

MATHEMATICAL FRAMEWORK

Momentum transport in the neutrally stratified ABL is governed by the incompressible Navier-Stokes equations. The wide range of length scales present in the ABL makes the direct solution of the Navier-Stokes equations unfeasible. The LES technique addresses this problem by low-pass filtering the Navier-Stokes equations removing all fluid motions below the LES filter scale Δ and then modeling the effect of these motions using a subgrid scale (SGS) model. Applying a low-pass filter to the nondimensional Navier-Stokes equations results in an unclosed set of partial differential equations of the form

$$\frac{\partial \tilde{u_i}}{\partial t} + \tilde{u_j}\left(\frac{\partial \tilde{u_i}}{\partial x_j} - \frac{\partial \tilde{u_j}}{\partial x_i}\right) = -\frac{\partial \tilde{p^*}}{\partial x_i} - \frac{\partial \tau_{ij}}{\partial x_j} + F_i. \tag{2.1}$$

The tilde in (2.1) refers to a variable filtered at scale Δ, $\tilde{u_i}$ is the filtered velocity in the i^{th} direction (1=streamwise, 2=spanwise, 3=vertical), x_i is the spatial coordinate in the i^{th} direction, $\tilde{p^*} = \tilde{p} + \frac{1}{2}\tilde{u_j}\tilde{u_j}$ is the filtered dynamic pressure, F_i is a generic forcing term, and $\tau_{ij} = \widetilde{u_i u_j} - \tilde{u_i}\tilde{u_j}$ is the SGS stress [26]. Equation (2.1) assumes an infinite Reynolds number such that viscous effects are neglected. Given the high Reynolds numbers typically encountered in atmospheric flows this assumption is reasonable. Equation (2.1) also assumes negligible rotational and thermal effects. Both of these assumptions are common in LES of canopy flows [52, 36, 50].

The SGS model selected for this study is the scale-dependent Lagrangian dynamic Smagorinsky model as developed by Stoll and Porté-Agel [37]. This model dynamically calculates the unknown model coefficient values using local flow features and a multiscale filtering approach along fluid particle trajectories. This model has been used successfully in other heterogeneous cases including flow over roughness changes in both neutral and stable atmospheric conditions [37][38][45]. This SGS model's ability to dynamically adjust to local flow conditions is critical for the study of flow around isolated trees where distinctly different flow regions with different integral length scales are expected.

The effects of the tree are included using the methodology developed by Yue et al. [52]. Under this methodology the approximate spatial arrangement of the tree is resolved as well as the local plant morphology. To address the local plant morphology, the nodes that the tree occupies are divided into two different categories, trunk nodes ("stem" nodes in Yue et al.) and leaf nodes. The nodes that the crown of the tree occupies are designated leaf nodes. For these nodes, a drag force d_i is applied to (2.1)

$$d_i = -C_d a(z) \tilde{u_i} |\tilde{u}| \tag{2.2}$$

where C_d is a drag coefficient, $a(z)$ is the leaf area density at a node, and $|\tilde{u}| = \sqrt{\tilde{u_j}\tilde{u_j}}$. The nodes that the trunk of the tree occupies are designated trunk nodes. For these nodes, a cylinder drag relation is added to (2.1)

$$f_i = -\frac{C_o D_{trunk}}{2\Delta_x \Delta_y} \tilde{u}_{o,i} |\tilde{u}_o| \tag{2.3}$$

where f_i is the added drag force, C_o is the cylinder drag coefficient, D_{trunk} is the diameter of the trunk, $\tilde{u}_{o,i}$ is the velocity at $3.5D_{trunk}$ upstream from the trunk, Δ_x and Δ_y are the grid spacing in the streamwise and spanwise directions respectively, and $|\tilde{u}_o|$ is the magnitude of the upstream velocity at the same location. In order to find the upstream velocity, a trilinear interpolation in terms of nearby velocity nodes is used. For more details on the plant drag model see Yue et al. [52]. The above relations assume that the impact of the tree's deformation on the forcing term it imposes is negligible. Given the relatively weak wind speeds employed in the present study this assumption is reasonable. For a more accurate model of the tree over a much broader range of velocities, the deformation of the tree would have to be considered in addition to the local plant morphology. The above relations also neglect the impact of small scale leaf motion on the flow field. These motions likely play an important role in the dynamics of fine scale turbulence within the canopy.

CHAPTER 3

NUMERICAL FRAMEWORK

The code used for this study is outlined in detail within Stoll and Porté-Agel [37]. The code solves the rotational filtered Navier-Stokes equations with additional tree related forcings (2.1)-(2.2) . A rectangular domain of volume $L_x L_y L_z$ is used for the study (see Figure 3.1). The domain is uniformly discretized in the streamwise (Δ_x spacing) and spanwise (Δ_y spacing) and vertical (Δ_z spacing) directions. The grid is collocated horizontally and staggered vertically with $\tilde{w}$ starting at $z = 0$ and all other variables ($\tilde{u}, \tilde{v}, \tilde{p^*}$) starting at $z = \frac{\Delta_z}{2}$. Horizontal derivatives are calculated using spectral methods. Vertical derivatives are calculated using central differencing. Time integration is conducted using a 2^{nd} order Adams-Bashforth scheme. The LES filter width size is $\Delta = (\Delta_x \Delta_y \Delta_z)^{1/3}$. For the dynamic procedure, the test filtering is conducted at 2Δ and 4Δ. The boundary conditions of the spanwise lateral boundaries are periodic. The boundary conditions of the streamwise lateral boundaries are set to be periodic with adjustments to account for the tree's wake. In order to ensure that the wake of the tree does not re-enter the domain, a buffer zone is implemented at the beginning of the domain. This buffer zone applies a force to the flow bringing the flow field from its exit condition to a velocity field flow plane extracted from a precursor simulation at each time step. A flow plane in this case is defined as a two-dimensional (2D) y-z slice of the 3D velocity field at an x location of the flow field. An example precursor flow plane at the end of the buffer zone is shown in Figure 3.1.

Within the buffer zone, the force applied is increased in magnitude in the streamwise direction by the function $F_{mag} = F(1-(0.5cos(\pi x/l)+0.5))$ where F_{mag} is the force applied, $l = 166$ m is the length of the buffer zone and F is the force required to bring the current velocity to the precursor flow plane value at the same y and z location. The library of flow planes is found using a precursor simulation of the same conditions without the tree and buffer zone. Similar methodology has been used successfully in LES of flow over bluff-bodies under neutral stratification and within numerous other LES cases [43, 16, 49, 44].

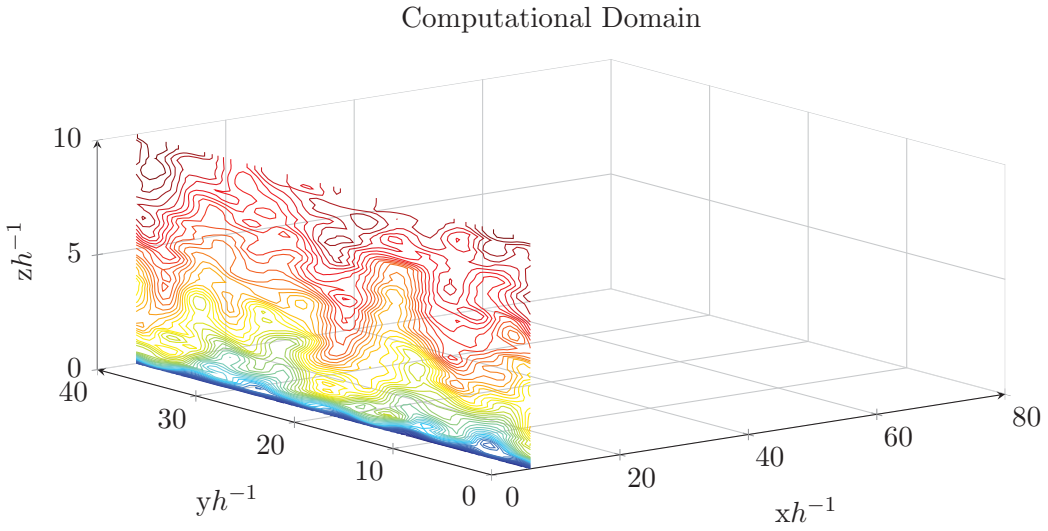

Figure 3.1. Computational domain nondimensionalized by tree height, h, with example instantaneous precursor flow plane velocity magnitude contours at the end of the inlet buffer zone.

One potential problem that can occur using this method is the formation of a development zone after the buffer zone. This is typically attributed to the necessity of the flow to adjust from incorrect flow planes to the correct flow features for the flow field [41]. In order to alleviate this problem the initial flow field of each simulation is taken from the precursor simulation at the first time step of flow plane collection. This ensures that the flow field transitions smoothly and accurately at the end of the buffer zone as the flow planes are changed.

The boundary condition imposed at the land surface is set by applying Monin-Obukhov theory at each point at the wall [37]. The top boundary condition is a zero-stress rigid lid. In dense canopy cases this top boundary conditions incorrectly impose a linearly decreasing momentum flux from the top of the canopy to a zero value at the top boundary [3]. In order to address this, the domain height is typically selected to be less than the boundary-layer height, but much greater than the canopy height [36, 52, 13]. While this is not an issue with the present case of flow around a single tree, these same basic guidelines are followed with $L_z = 10h$, where h is the height of the tree.

The spanwise, $L_x = 80h$ and streamwise, $L_y = 40h$, lengths of the domain are loosely based on results for the related case of flow over wind turbines in the ABL. Previously it has been found that the influence of a turbine is still discernible 20 rotor heights downstream [31]. In order to error on the side of greater wake dissipation, and to allow space for possible flow development between the buffer zone and the tree, a safety factor of 4 is used on this value for L_x. The spanwise dimension, L_y, of the domain is selected semi-arbitrarily to be a large enough value to ensure that there is little to no possibility of the wake reaching the sides of the domain, and to ensure that the domain is large enough to create a realistic ABL. A summary of the domain characteristics is given in Table 3.1. Figure 3.1 depicts the domain with an example instantaneous precursor flow plane.

Table 3.1. LES Inputs Information

Neutral Case				
$L_xL_yL_z$	$N_xN_yN_z$	z_o	l	P_{const}
1600*800*200 m^3	144*72*72	0.01 m	166 m	5.22*10^{-4} m/s^2

3.1 Tree Parameterization

This study focuses on broad leaf deciduous trees. In particular, flow around a Red Maple is simulated. The Red Maple tree is selected due to its tolerance to a very wide range of

climatic conditions, its general abundance, and its similarity to a wide range of deciduous trees. In order to specify the height, trunk diameter, and crown diameter, or spread, values were obtained from reported value ranges typical of Red Maple trees [17]. Values near the middle of the given ranges are used in order to model a typical red maple tree. The leaf area density of the tree, $a(z)$, is defined by an empirically derived model [6]. The form of the model is

$$a(z) = L_m \left(\frac{h - z_m}{h - z} \right)^n exp\left[n\left(1 - \frac{h - z_m}{h - z} \right) \right] \tag{3.1}$$

where

$$n = \begin{cases} 6 & \text{if } 0 \leq z < z_m \\ 1/2 & \text{if } z_m \leq z \leq h \end{cases}$$

In this model, L_m is the maximum $a(z)$ value and z_m is the height at which L_m is located [6]. A summary of all parameters used for the tree in the present study can be found in Table 3.2. Figure 3.2 depicts the LAD profile from (3.1) using the parameters given in Table 3.2.

Three different $z_m = 0.3h, 0.5h, 0.7h$ values are simulated. For the three cases $L_m = 0.6, 0.5, 0.44$ was scaled until the leaf area index (LAI) of each tree was equal to 5.0, where LAI is defined as LAI$= \int a(z)dz$. This value of LAI corresponds to a typical value found in deciduous forests [33, 4]. The value of the drag coefficient of the canopy, C_d, used is 0.15. This value has been found to be appropriate in measurements and studies conducted on deciduous forests [39, 36, 15]. The value of the drag coefficient of the trunk, C_o, used is 1.0. This value is approximately the values found for flow around a cylinder at high Reynolds numbers [34] and is also the value used previously with (3.1) for the stocks of corn plants [52]. If the drag force resulting from the $a(z)$ from equation (3.1) is high enough it is possible that a sharp transition in velocity could occur within the tree. When using spectral methods a sudden change in velocity can cause the onset of Gibbs phenomena at the edges of the transition. This is undesirable since it adds unphysical undulations in the flow field. In order to reduce the likelihood of such undulations and to account for the 3D structure of the tree, the LAD was tapered radially from the center of the tree assuming a normal distribution of LAD. This ensures that the forcing due to the tree is more gradually applied, lessening the possibility of Gibbs phenomena.

Figure 3.3 shows a basic view of the 3D geometry of the model trees used in the simulations. The trunk diameter, D_{trunk}, and the crown diameter, D_{crown}, are taken from reference data [17]. The height of the trunk, h_{trunk}, is set equal to the height at which the LAD is 20 percent of L_m. The location of the tree within the domain is centered, $20h$ from domain edge, in the spanwise direction and is $x_{tree} = 20h$ streamwise from the inlet.

Table 3.2. Tree Parameter Information

h	D_{trunk}	D_{crown}	h_{trunk}	LAI	z_m	L_m
20 m	0.6 m	12 m	6 m	5.0	0.7h, 0.5h, 0.3h m	0.6, 0.5, 0.44 m^2/m^3

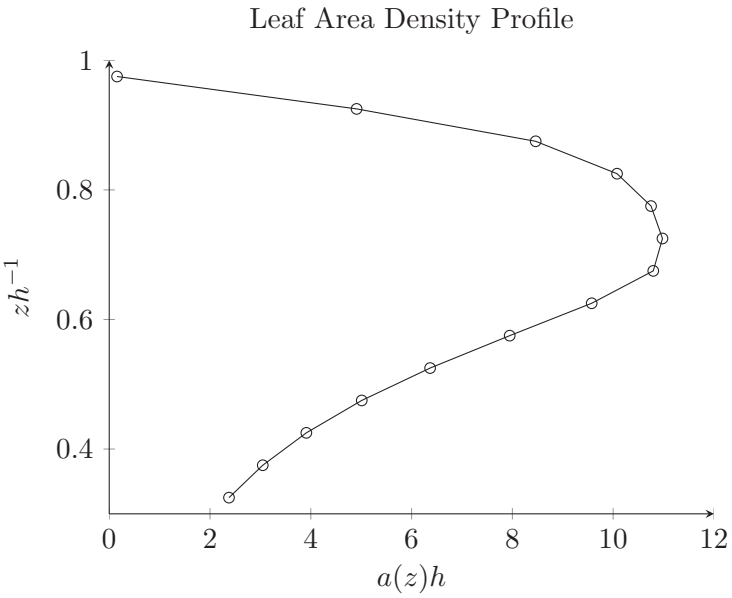

Figure 3.2. Leaf area density, $a(z)$, profile of the tree canopy nondimensionalized by tree height h.

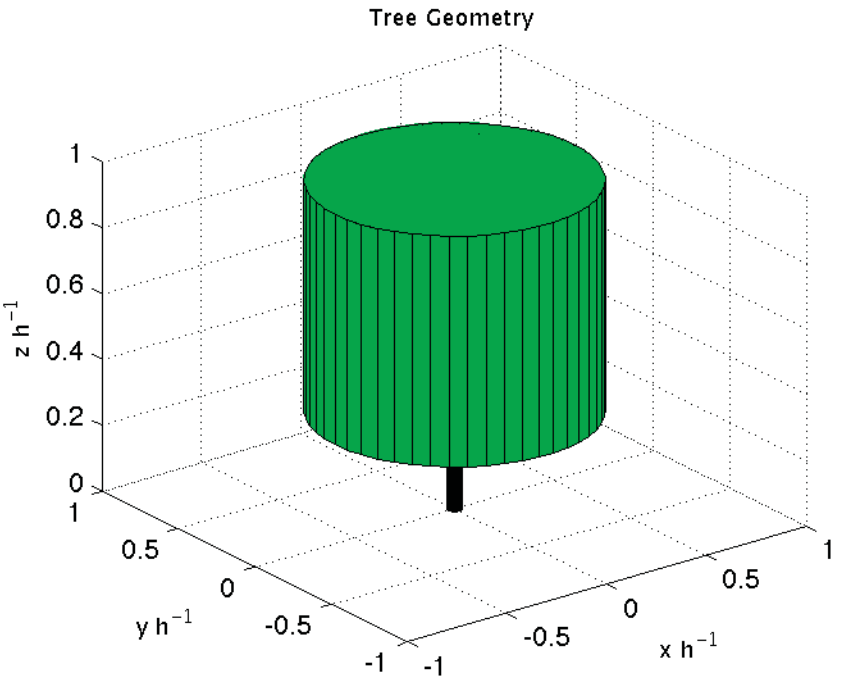

Figure 3.3. Tree geometry. Green indicates volume containing leaf nodes; brown indicates volume containing trunk nodes.

As indicated in Table 3.1, the number of grid points was set to $N_x N_y N_z = 144 * 72 * 72$ for the volume $L_x L_y L_z = 1600 * 800 * 800$ m^3. The resulting grid spacings from this setup are $\Delta_x = 11.11$ m, $\Delta_y = 11.11$ m, and $\Delta_z = 2.82$ m. To initialize the precursor simulation the streamwise velocity was set using a log law relation

$$u(z) = \frac{u_*}{k}\left(ln(\frac{z}{z_o})\right)$$

where $u(z)$ is the initial velocity at vertical level z, $u_* = 0.323$ m/s is the friction velocity, $z_o = 0.01$ m is the surface roughness and $k = 0.4$ is the Von Kármán constant. The friction velocity is found by assuming that the flow is quasi-steady such that $u_* = \sqrt{P_{const} L_z}$. The spanwise and vertical initial velocities are set to a value of 0 everywhere within the field. In order to introduce turbulence into the flow field random noise with a maximum magnitude of $u_{noise} = 0.25 u_*$ is added to all three velocity components in the lower 25 percent of the domain. The velocity field is simulated from this initial state with a constant pressure forcing, $P_{const} = 5.22{*}10^{-4}$ m/s^2. Once the precursor simulation reaches a quasi steady-state, a tree and the buffer zone are introduced ito the domain. Three trees are simulated separately with $z_m = 0.3h, 0.5h, 0.7h$ and a LAI = 5. Results for each tree are taken over a one-hour period.

CHAPTER 4

RESULTS AND DISCUSSION

We begin by exploring the time averaged mean velocity components. The nondimensionalized momentum statistics for the three cases are qualitatively similar. In order to reduce redundant information, only the $z_m = 0.7h$ case momentum field results are shown. This case is selected for presentation because of the relatively common occurrence of $z_m = 0.7h$ in maple trees compared to the other cases simulated [6]. Velocities are nondimensionalized by the friction velocity $u_* = 0.323$ m/s and lengths are nondimensionalized by tree height h. To highlight the impact of the tree on the mean velocity, a velocity defect is used. The velocity defect used here is defined as $u_d = -u_i + u_{i,inlet}$ where u_d is the velocity defect, u_i is the i^{th} velocity component and $u_{i,inlet}$ is the i^{th} velocity value of the spanwise averaged, mean inlet velocity profile at the same vertical level as u_i. Detailed descriptions of the inlet profiles used in all defect definitions can be found in Stoll and Porté-Agel [37]. In addition to the velocity defect plots, the unaltered horizontal and vertical profiles of mean velocity are also presented. The locations selected to create these profiles are the locations of maximum LAD, y_m and z_m. The maximum y location, y_m, is located through the centerline of the tree.

Figure 4.1 depicts the mean streamwise velocity for the $z_m = 0.7h$ case. The vertical streamwise profiles, horizontal profiles, and defect contours all depict a region of velocity defect centered near $z_m = 0.7h$. The defect decreases in magnitude in the streamwise direction in a similar manner to the velocity defect on the downstream side of a windbreak or in a pure plane wake flow. In windbreak flows, the inlet flow experiences a section of slow bleed flow across the cross-section of the windbreak with a strong flow displacement at the top of the windbreak [22]. These two types of flow mix and then enter a re-equilibrium zone bringing the statistics of the flow back to their inlet values. Qualitatively, the major difference between the streamwise velocity results presented in Figure 4.1 and traditional windbreak flows is the presence of 3D geometrical influence. The 3D nature of flow around an isolated tree results in extra displacement zones at the edges of the crown.

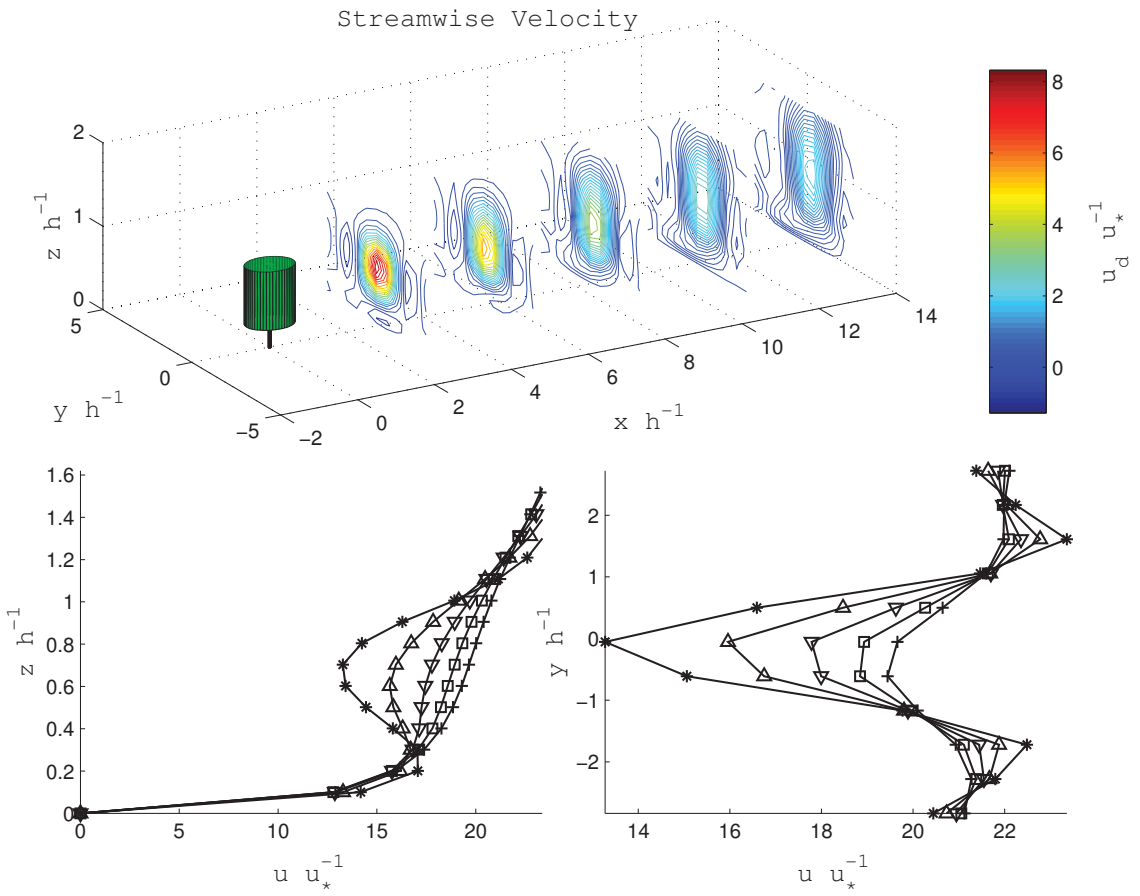

Figure 4.1. Nondimensional streamwise velocity profiles and velocity defect contours around the tree. The top panel shows defect contours taken at several x locations downstream. The bottom left panel depicts vertical profiles taken through the center of the tree at the same x locations as the contours. The bottom right panel depicts horizontal profiles through $z = 0.7h$ at the same x locations of the contours. x $h^{-1} = 2.77$ (*), x $h^{-1} = 5.55$ ($\triangle$), x $h^{-1} = 8.33$ (∇), x $h^{-1} = 11.11$ ($\square$), x $h^{-1} = 13.88$ (+).

The velocity defect contours also show a mixing zone that expands in the horizontal and vertical directions downstream of the tree. Examining the streamwise velocity defect contours, it is observed that the general shape of the streamwise velocity defect is seen to be roughly Gaussian. This is similar to results for an axisymmetric wake [30]. Qualitatively, it is also observed that the shape of the streamwise velocity defect is wider than it is tall. This suggests that a Gaussian description of the velocity defect would need to account for different spreads in the vertical and spanwise directions.

Figure 4.2 depicts the mean spanwise velocity. In the horizontal profiles, two regions of increased spanwise velocity magnitude are observed. These regions bring fluid inwards towards the wake fueling its increase in size. The spanwise velocity defect contours illustrate the 3D nature of these regions with the regions extending to near the top and bottom of the crown of the tree. The general shape of the spanwise velocity in the wake region is not symmetric. This is assumed to be a numerical artifact due to using too short of an averaging time. The horizontal profiles in the lower right panel have a similar shape to horizontal transects through plane and axisymmetric wakes [1]. Unlike the horizontal transects, the vertical profiles in the lower left panel of Figure 4.2 do now show a clear signature of the tree in the downstream direction. The magnitude of the spanwise velocity defect is found to be quite small compared to the magnitude of the streamwsie velocity defect.

The mean vertical velocity is depicted in Figure 4.3. Similar to the spanwise wake velocity the mean vertical velocity also brings the flow inwards to the wake in the vertical direction. Examining the vertical profiles in the lower right panel of Figure 4.3, it is observed that the vertical velocity profiles exhibit similar behavior to that of a plane or axisymmetric wake [1]. Like the spanwise velocity, the magnitude of the vertical velocity defect is quite small compared to the streamwise velocity defect. The vertical velocity returns to its upstream undisturbed profile within a shorter downstream distance than the spanwise velocity.

The total time averaged nondimensionalized $u'w' = u'w'$ stress including both resolved and subgrid contributions around the tree is shown in Figure 4.4. In order to study the impact of the tree on this stress a defect definition is used. This definition is much the same as that used for the mean streamwise velocity being defined as $u'w'_d = -u'w' + u'w'_{inlet}$. In this definition $u'w'$ is the stress at the location of interest and $u'w'_{inlet}$ is the corresponding stress value of the spanwise averaged, mean inlet vertical turbulent stress. Unaltered profiles are also presented in Figure 4.4 in the same format as the mean velocity.

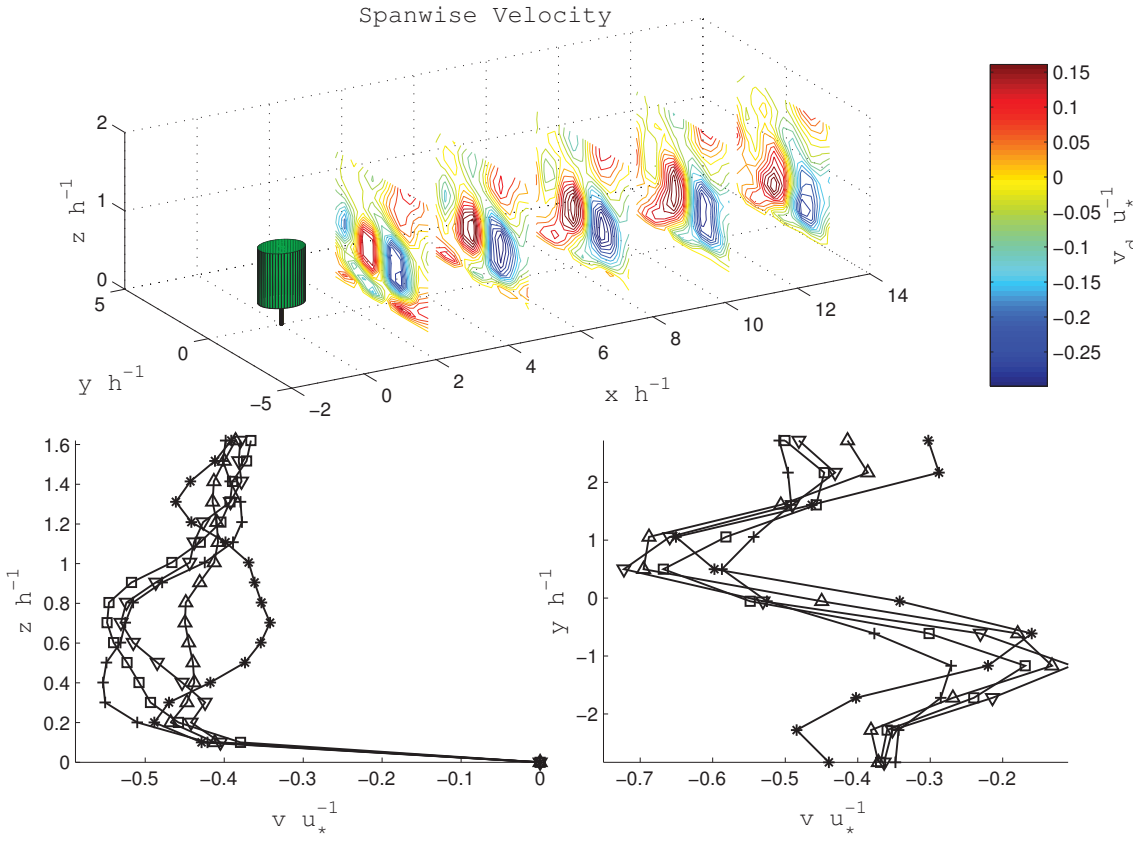

Figure 4.2. Nondimensional spanwise velocity profiles and velocity defect contours around the tree. The top panel shows defect contours taken at several x locations downstream. The bottom left panel depicts vertical profiles taken through the center of the tree at the same x locations as the contours. The bottom right panel depicts horizontal profiles through $z = 0.7h$ at the same x locations of the contours. x $h^{-1} = 2.77$ (*), x $h^{-1} = 5.55$ ($\triangle$), x $h^{-1} = 8.33$ (∇), x $h^{-1} = 11.11$ ($\square$), x $h^{-1} = 13.88$ (+).

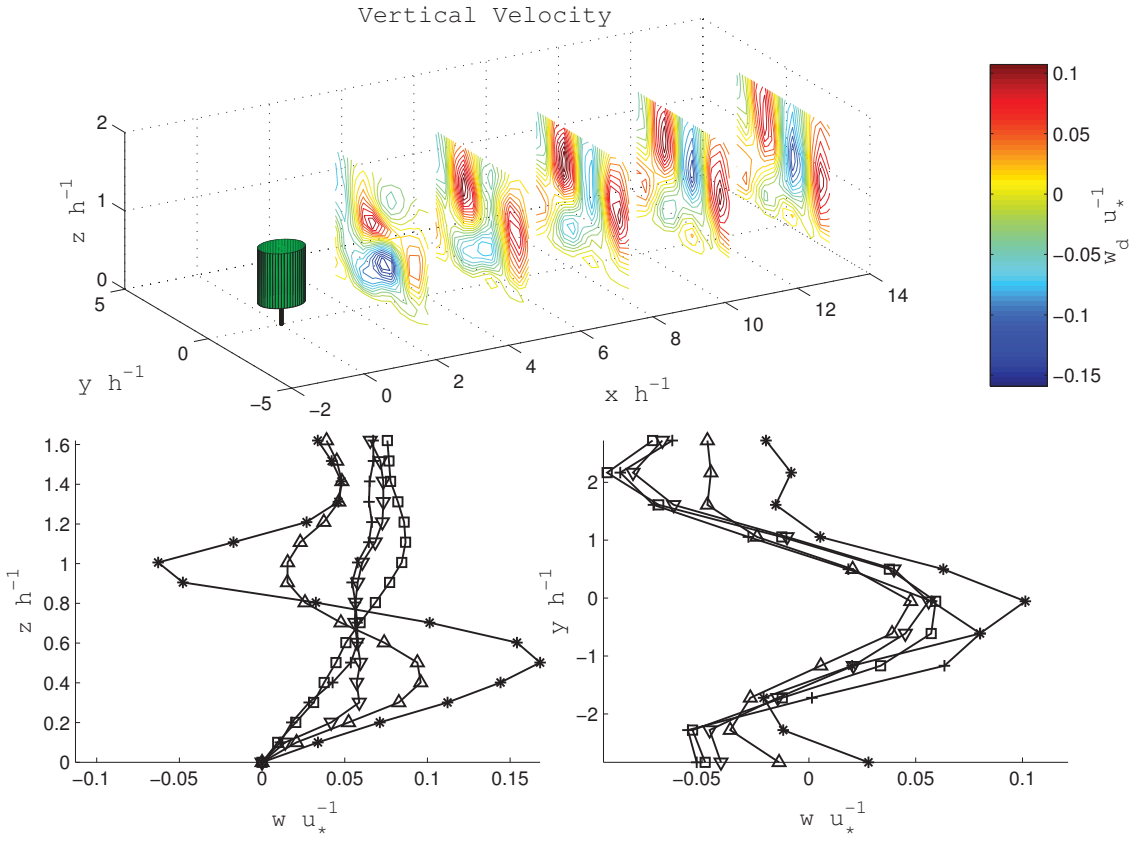

Figure 4.3. Nondimensional vertical velocity profiles and velocity defect contours around the tree. The top panel shows defect contours taken at several x locations downstream. The bottom left panel depicts vertical profiles taken through the center of the tree at the same x locations as the contours. The bottom right panel depicts horizontal profiles through $z = 0.7h$ at the same x locations of the contours. x $h^{-1} = 2.77$ (*), x $h^{-1} = 5.55$ ($\triangle$), x $h^{-1} = 8.33$ (∇), x $h^{-1} = 11.11$ ($\square$), x $h^{-1} = 13.88$ (+).

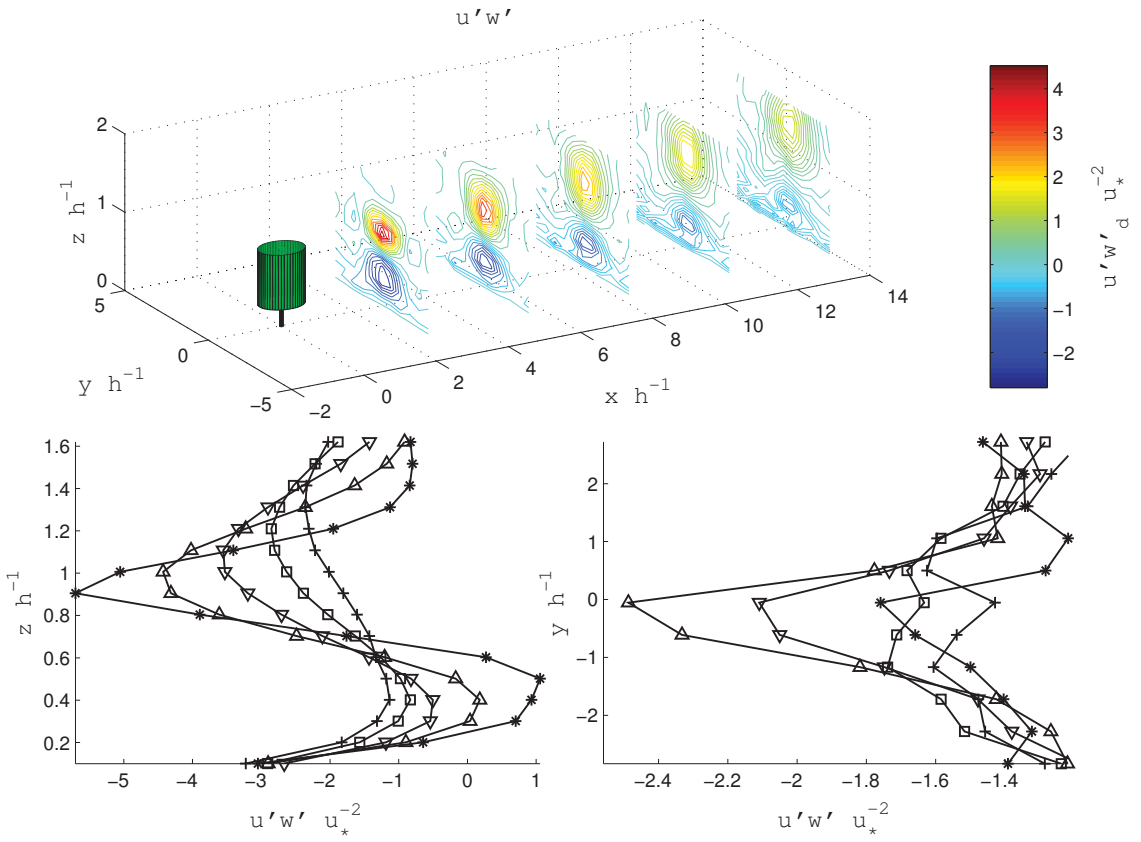

Figure 4.4. Nondimensional $u'w'$ profiles and defect contours around the tree. The top panel shows defect contours taken at several x locations downstream. The bottom left panel depicts vertical profiles taken through the center of the tree at the same x locations as the contours. The bottom right panel depicts horizontal profiles through $z = 0.7h$ at the same x locations of the contours. x $h^{-1} = 2.77$ (*), x $h^{-1} = 5.55$ ($\triangle$), x $h^{-1} = 8.33$ (∇), x $h^{-1} = 11.11$ ($\square$), x $h^{-1} = 13.88$ (+).

The vertical profiles of $u'w'$ exhibit a section of strong negative stress values near the top of the tree. Within the vertical profiles of $u'w'$ a region of positive stress is found at the bottom of the crown, near the tree. The $u'w'_d$ contours depicts a region of greatly heightened stress defect near the top of the tree with a region of negative stress defect near the tree. The strong negative stress values near the top are attributed to the tree enhancing turbulent mixing, bringing fluid from above the tree towards the ground. The drawing of fluid into the wake region due to the enhanced turbulence mixing from the tree contributes to the growth of turbulence within the wake region. The positive values of vertical stress near the ground, next to the tree are attributed to the tree enhancing turbulent mixing which then reduces the transport of the momentum to the ground. These two effects dissipate with downstream distance. The turbulent stress distribution observed in the $u'w'_d$ contours is similar to that within an axisymmetric wake [1]. Both have two peaks inwards of the edge of the wake with zero vertical stress values occurring near the center of the wake and at the wake's edges. This zero crossing of stress values has also been seen in previous work studying flow around isolated trees [2].

Figure 4.5 shows the total horizontal stress. A stress defect is again utilized to illustrate the impact of the tree on the stress. Unaltered profiles are additionally shown in both the vertical and horizontal directions. As can be seen in the horizontal profile plots and within the contour plots of defect there is a region of both decreased and increased horizontal stress that spans outwards downstream. Both of these regions indicate turbulent transport horizontally into the wake. The turbulent transport into the wake horizontally is attributed to the enhanced turbulent mixing due to the tree. The general shape of the distribution of $u'v'_d$ is similar to that of an axisymmetric wake [1].

Resolved nondimensionalized streamwise velocity variance u'^2 in the vicinity of the tree is depicted in Figure 4.6 and the total turbulent kinetic energy TKE=$u'^2 + v'^2 + w'^2$ is depicted in Figure 4.7. A region of heightened u'^2 and TKE is shown to form near the region of maximum LAD and to span outwards in a similar fashion to the streamwise velocity defect. Comparing Figure 4.6 and Figure 4.7, it is clear that the u'^2 stress component is the major contributor to the TKE accounting for approximately 85-90 percent of the total TKE. From Figure 4.6, it is observed in the u'^2_d contours that u'^2_d follows a roughly Gaussian shape. Similar to the streamwise velocity defect, it is seen that this roughly Gaussian shape is nonsymmetric.

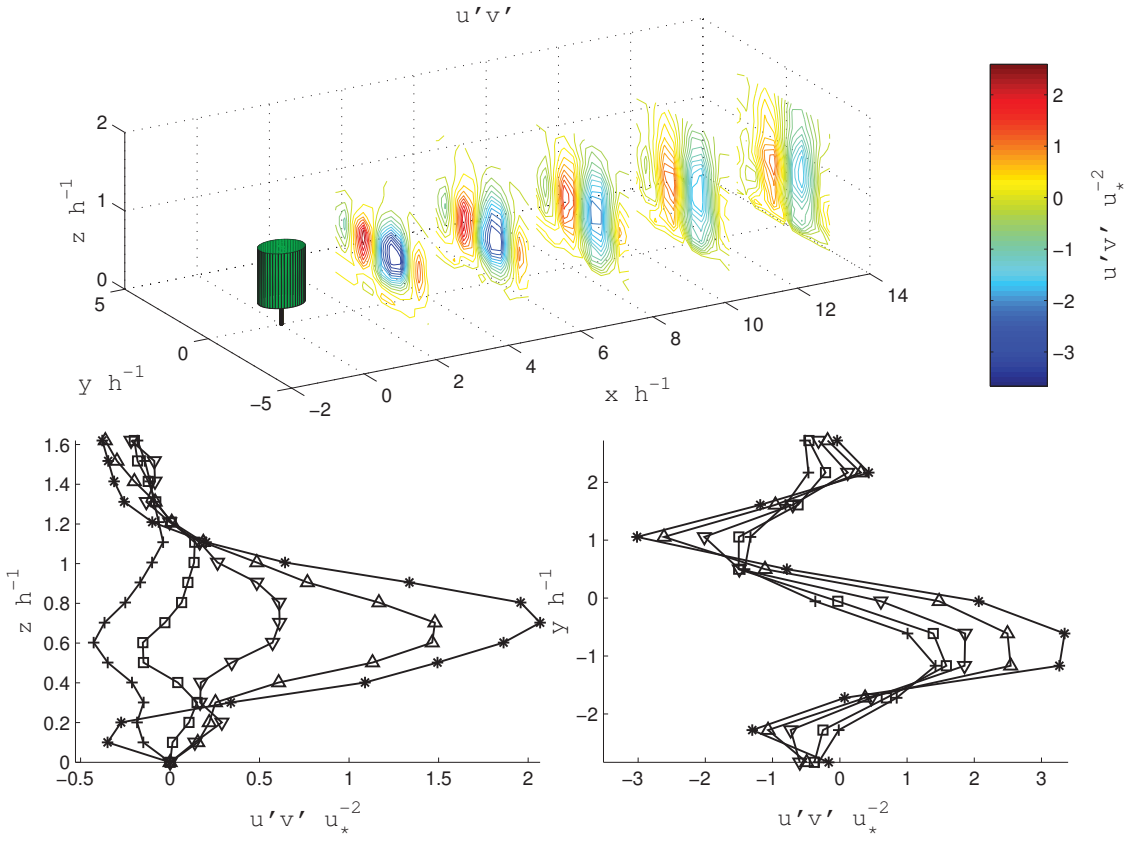

Figure 4.5. Nondimensional $u'v'$ profiles and defect contours around the tree. The top panel shows defect contours taken at several x locations downstream. The bottom left panel depicts vertical profiles taken through the center of the tree at the same x locations as the contours. The bottom right panel depicts horizontal profiles through $z = 0.7h$ at the same x locations of the contours. x h^{-1} = 2.77 (*), x h^{-1} = 5.55 ($\triangle$), x h^{-1} = 8.33 (∇), x h^{-1} = 11.11 ($\square$), x h^{-1} = 13.88 (+).

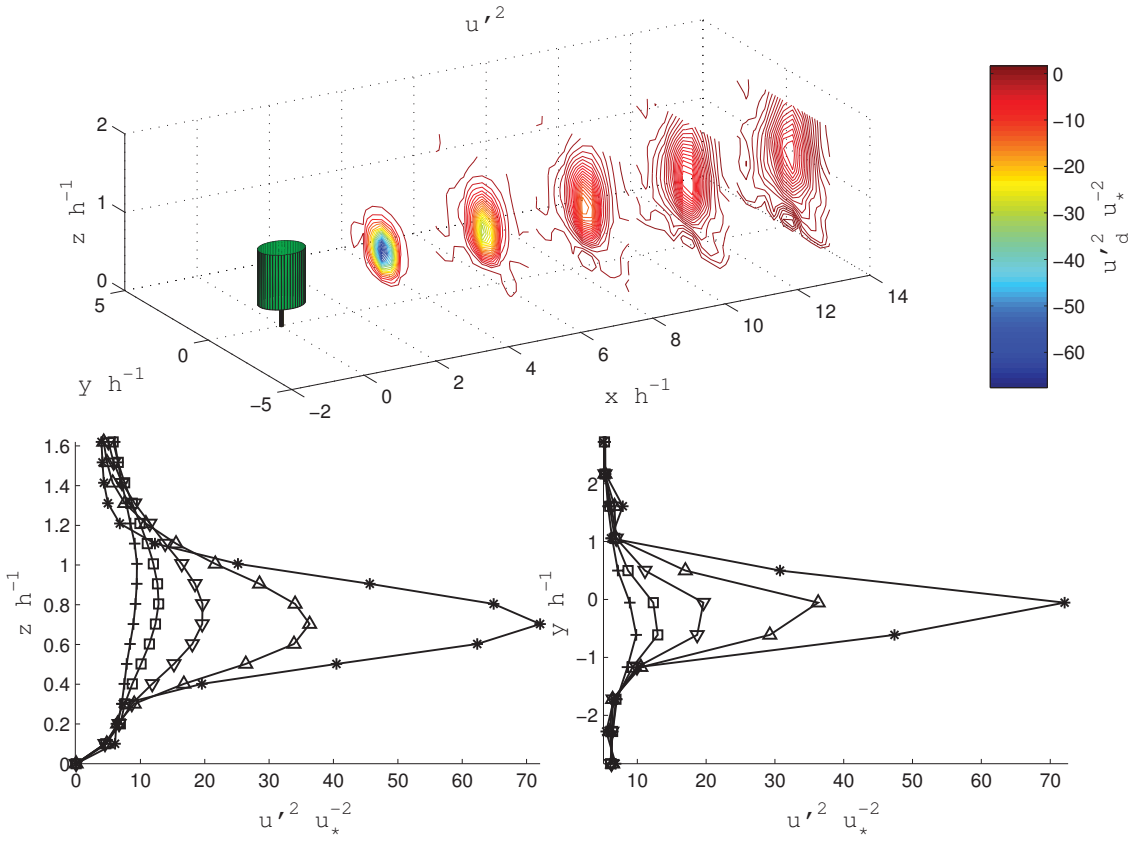

Figure 4.6. Nondimensional u'^2 profiles and defect contours around the tree. The top panel shows defect contours taken at several x locations downstream. The bottom left panel depicts vertical profiles taken through the center of the tree at the same x locations as the contours. The bottom right panel depicts horizontal profiles through $z = 0.7h$ at the same x locations of the contours. x $h^{-1} = 2.77$ (*), x $h^{-1} = 5.55$ ($\triangle$), x $h^{-1} = 8.33$ (∇), x $h^{-1} = 11.11$ ($\square$), x $h^{-1} = 13.88$ (+).

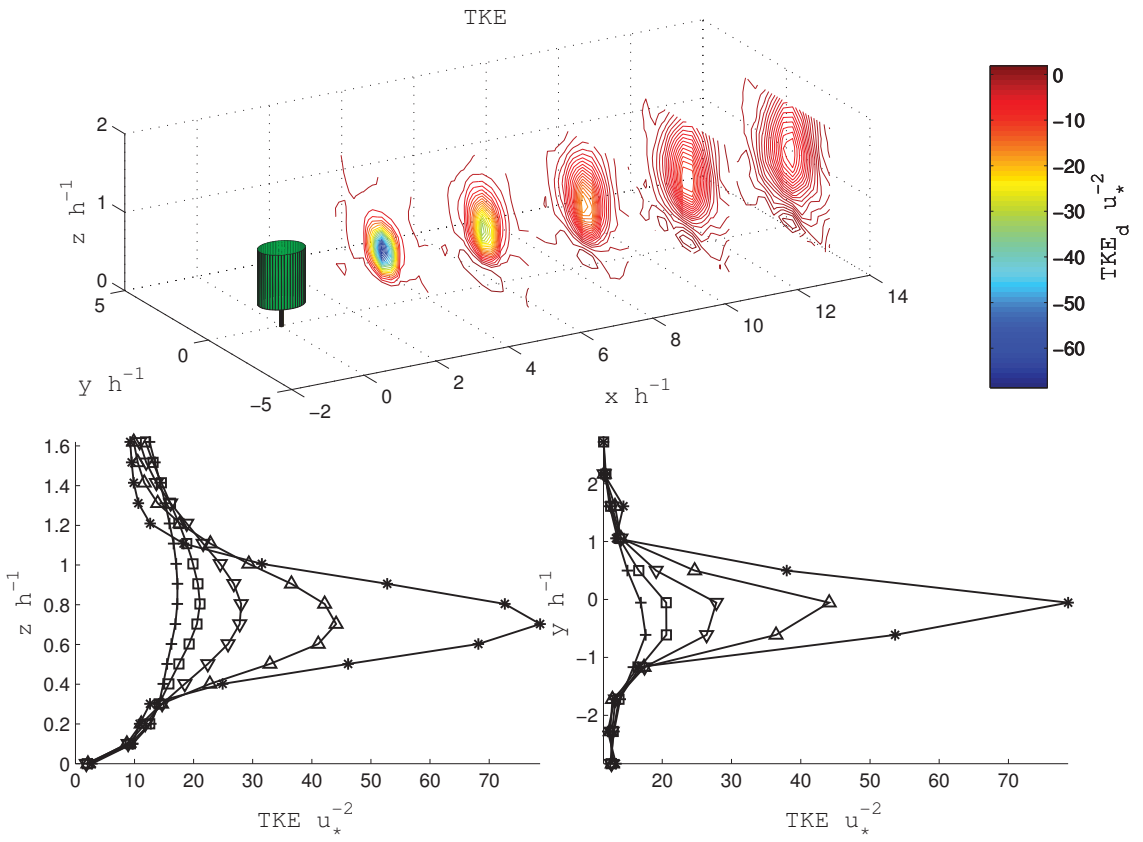

Figure 4.7. Nondimensional turbulent kinetic energy profiles and defect contours around the tree. The top panel shows defect contours taken at several x locations downstream. The bottom left panel depicts vertical profiles taken through the center of the tree at the same x locations as the contours. The bottom right panel depicts horizontal profiles through $z = 0.7h$ at the same x locations of the contours. x $h^{-1} = 2.77$ (*), x $h^{-1} = 5.55$ ($\triangle$), x $h^{-1} = 8.33$ (∇), x $h^{-1} = 11.11$ ($\square$), x $h^{-1} = 13.88$ (+).

4.1 Model Creation

Canopy dispersion and momentum transport models used for forestry, agricultural, and urban applications require efficient parameterizations based largely on the geometry of the problem. In this section, a simple empirical model for use in these types of applications is proposed. The model replicates the basic features of the mean velocity, turbulent stresses and turbulent variances. It is based on the well-known set of analytical equations for an axisymmetrical wake [1, 30, 9]. An axisymmetrical wake was chosen as a basis for the model due to the similarities between the mean flow and turbulent stress features shown in section 4.1 and classical axisymmetrical wakes. The new tree wake model starts at the location of maximum LAD and spreads outwards according to modified axisymmetric wake equations.

The averaged equation of motion for an axisymmetric wake in cylindrical coordinates is

$$\overline{u}\frac{\partial \overline{u}}{\partial x} + \frac{1}{r}\frac{\partial r\overline{u'u'_r}}{\partial r} = 0 \tag{4.1}$$

where r is the nondimensional radial location from the center of the wake, and $\overline{u'u'_r}$ is the radial turbulent stress [1]. Equation (4.1) assumes a statistically steady state, negligible viscous effects, and negligible pressure gradients. It was previously observed that the spanwise (Figure 4.2) and vertical (Figure 4.3) velocity defects are small in value when compared to the streamwise (Figure 4.1) velocity defect. Because of this, it is assumed that the outward radial velocity component $\overline{u_r}$ is negligible. Assuming that the velocity defect is a Gaussian, the streamwise velocity is defined as

$$\overline{u} = u_o - u_c \exp(\frac{-r^2}{\lambda^2\delta^2}) \tag{4.2}$$

where u_o is a characteristic convective velocity set to the inlet velocity profile, u_c is the velocity defect at the center of the Gaussian distribution, δ is the wake width, and λ is a scaling constant for δ. Typically δ is assumed to be dependent on only x [30]. It was previously found that the streamwise velocity, Figure 4.2, has a roughly Gaussian shape that is wider than it is tall. Due to this the wake width is set to vary with θ and x such that $\delta = f(x, \theta)$. u_c for this case is taken to vary with only x as is traditionally done for plane and axisymmetric wakes [9]. In order to designate λ, the plume half width is set such that $u_d(x, \delta(x, \theta)/2, \theta) = 0.05u_d(x, 0, \theta)$ where $u_d = f(x, r, \theta)$ is the velocity defect defined as

$$u_d = u_c \exp(\frac{-r^2}{\lambda^2\delta^2}) \tag{4.3}$$

Using this definition, $\lambda^2 = 0.083$.

In order to use (4.3) it is necessary to find functions of δ and u_c. A function for δ is constructed using the simulation data. First δ is measured by identifying the radial point

$r = \delta/2$ such that $u_d(x, r, \theta) = 0.05u_c$ with $u_c = u_d(x, 0, \theta)$. The LES measured δ values are used to find a functional form for δ to use in (4.3). To account for the near and far wake behavior behind the tree, the equation describing δ is changed depending on region. The far wake is set to locations at which $\frac{u_o}{u_c} < 0.5$. Using this definition it is defined from the LES results that all locations past 7.77 tree heights are the far wake region. This separation point between the near and far wake regions is found to provide reasonable agreement between modeled statistics and simulation results. Within the near wake region, it is found that a linear relationship provides a good fit for δ. Within the far wake region a general power law is found to give reasonable accuracy, as has been found for plane and axisymmetric wakes [30]. To account for the θ dependence in δ, a constant amplitude cosine formulation is used with $\delta = Acos(2\theta) + B(x)$ where$A$ is half of the average difference between the spanwise and vertical δ values and $B(x)$ is the midpoint between the spanwise and vertical δ values, such that $B(x) = (\delta(x, 0) - \delta(x, \pi/2))/2$. The resulting equations for δ in the near and far wake regimes are as follows

$$\delta/h = 1.15cos(2\theta) + B/h$$

where

$$\begin{aligned} B/h &= 0.05(x/h) + 2.22 \quad \text{if } x/h < 7.77 \\ B/h &= 1.70(x/h)^{0.19} \quad \text{if } x/h \geq 7.77 \end{aligned} \tag{4.4}$$

A functional relationship for the centerline velocity u_c is determined by the same methodology used for δ. This was accomplished by fitting measured values of u_c from the simulations as a function of the streamwise distance from the tree. Like δ, it is found that within the near wake a linear relationship provides reasonable accuracy, and a power law works well in the far wake. The far wake power law behavior of u_c is similar to results from plane and axisymmetric wakes [30]. An example fit for δ is depicted in Figure 4.8. An example fit for u_c is depicted in Figure 4.9. The resulting equations for u_c from a least squares regression analysis of measurements of u_c in the near and far wake regimes are as follows

$$\begin{aligned} u_c/u_* &= -0.63(x/h) + 9.33 \quad \text{if } x/h < 7.77 \\ u_c/u_* &= 90.68(x/h)^{-1.48} \quad \text{if } x/h \geq 7.77 \end{aligned}$$

According to experimental results in the far wake regime of an axisymmetric wake $u_c \sim x^{-2/3}$ and $\delta \sim x^{1/3}$ [9, 30]. In Equation (4.1) it is seen that $u_c \sim x^{-3/2}$. The greater negative power indicates that the peak velocity defect value decreases faster with downstream distance than that of an axisymmetric wake in the far wake region. In Equation (4.4) $\delta \sim x^{0.2}$ which is fairly comparable, but slightly less than wake spread results for an axisymmetric wake in the far wake region.

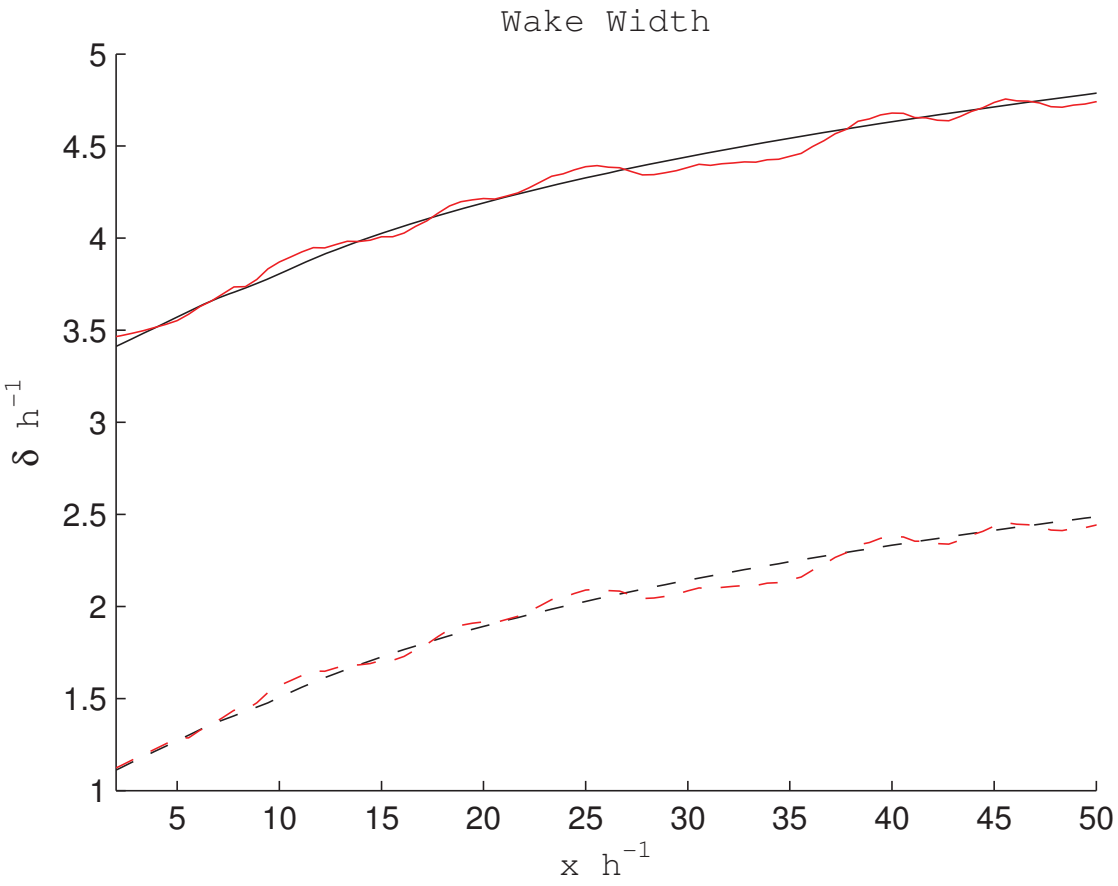

Figure 4.8. Example wake width from $z_m = 0.7h$ simulation data and corresponding data fits with downstream distance. (−) Horizontal width from simulation, (−) Horizontal width from fit, (−−) Vertical width from simulation, (−−) Vertical width from fit.

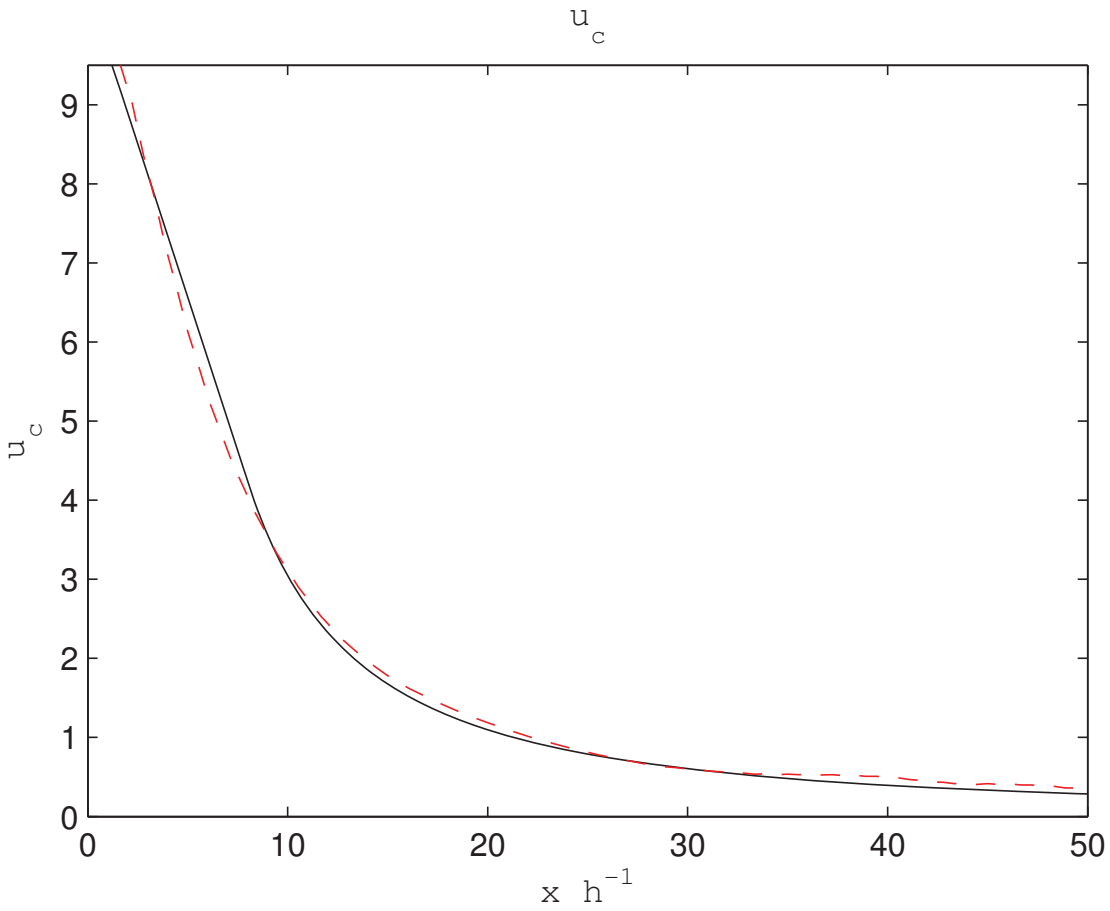

Figure 4.9. Example maximum velocity deficit from $z_m = 0.7h$ simulation data and from corresponding data fit with downstream distance. (−−) Simulation data, (−) Data fit.

The nondimensional velocity defect relationships given by Equations (4.4) and (4.1) are shown in Figure 4.10 at several locations downstream from the tree. The figure depicts both spanwise and vertical transects through the wake from the model and the simulation. Overall, the model is shown to depict the velocity defect in the spanwise and vertical direction with good accuracy. There are a few exceptions to this. In the near vicinity of the tree, the model does not include the flow displacement regions in the horizontal profile. This results in the model not capturing the negative velocity defect regions at the edge of the wake in the near tree region. In the vertical profiles, the model slightly underpredicts the spread of the distribution in the vertical direction downstream from the tree.

In section 4.1 it was noted that the u'^2 variance dominates the TKE, Figure 4.6, was significantly altered by the presence of the tree. Given this the model assumes u'^2 =TKE, such that the other variances are neglected. In general, the shape of the TKE defect in the wake region is very similar to the streamwise defect. Based on this an equation similar to eqref9 is assumed for the TKE

$$TKE_d = \kappa exp(\frac{-r^2}{\lambda^2 \delta^2}) \tag{4.5}$$

where TKE_d is the TKE defect and κ is a scaling parameter similar to u_c. A functional form for κ is found based on simulation data in the same manner as for u_c. The resulting equations for κ in the near and far wake regions are

$$\begin{array}{rl} \kappa/u_*^2 = -10.47(x/h) + 97.91 & \text{if } x/h < 7.77 \\ \kappa/u_*^2 = 470.9451(x/h)^{-1.63} & \text{if } x/h \geq 7.77. \end{array} \tag{4.6}$$

Figure 4.11 shows the model given by equations (4.5) and (4.6) compared to the simulation results. The model is found reproduces TKE defect in both the vertical and spanwise direction with moderate accuracy. There are some notable discrepancies between the model results and the simulation results. The model is observed to overpredict the values of TKE near the tree. This overprediction is largely the result of the overprediction of the horizontal spread of TKE within the model.

Typically in order to analyze the stresses of an axisymmetric wake (4.2) is substituted into (4.1), with the assumption that $\delta \sim x^{1/3}$ and $u_c \sim x^{-2/3}$ [1]. The solution of the resulting differential equation is

$$\overline{u'u'_r} = \frac{-ru_o u_c}{3x} \exp(\frac{-r^2}{\lambda^2 \delta^2}) \tag{4.7}$$

Given the complex forms used for δ and u_c it becomes unwieldy to calculate and utilize a true analytical result to calculate the momentum stress. In section 4.1 it was found that the momentum stress in the tree wake zone (Figures 4.4 and 4.5, respectively) qualitatively has a similar shape to that suggested by (4.7).

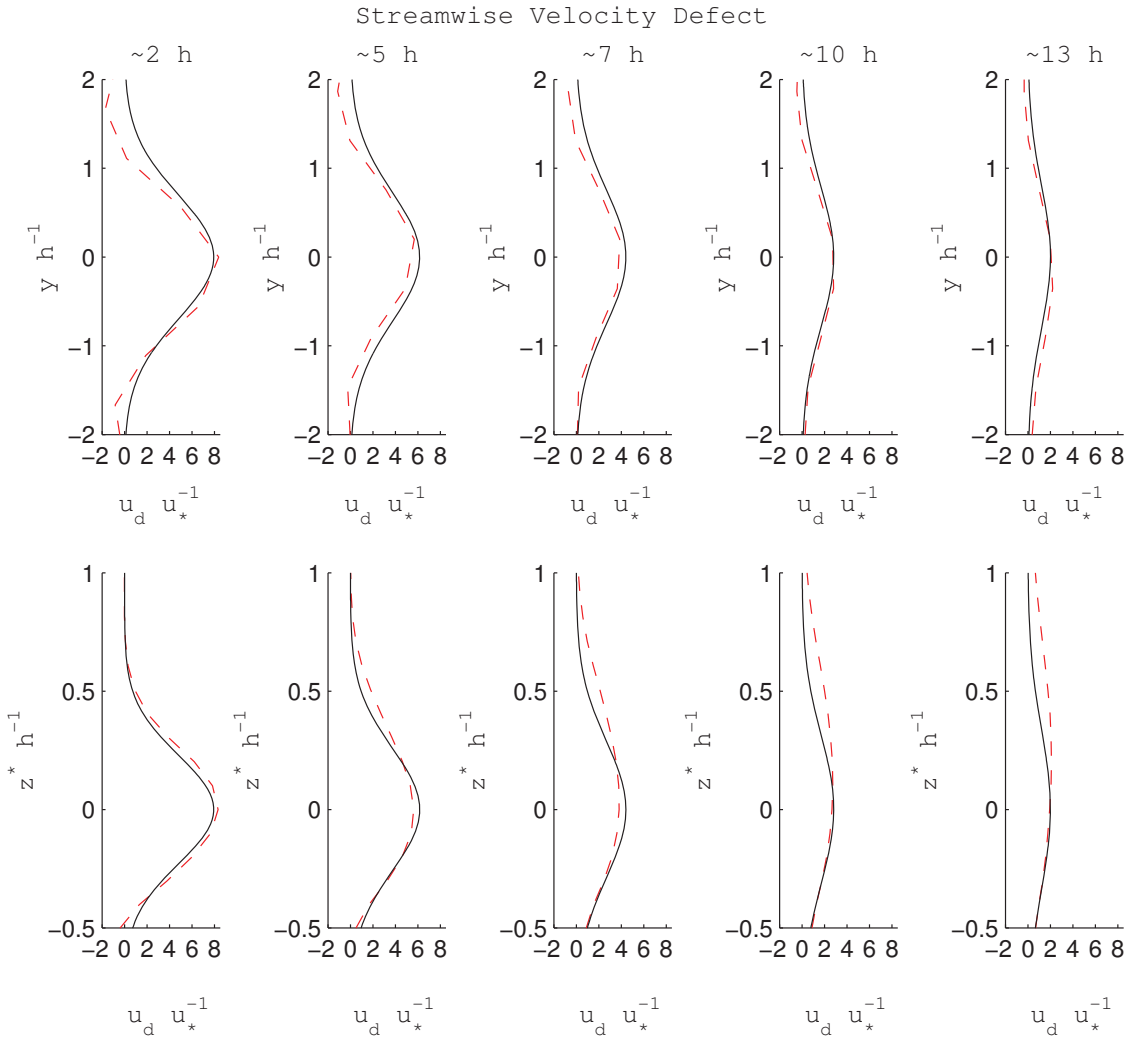

Figure 4.10. Streamwise velocity defect at several x locations downstream of tree from simulation and from constructed model with $z^* = z - z_m$ and $z_m = 0.7h$. (−−) Simulation, (−) Model.

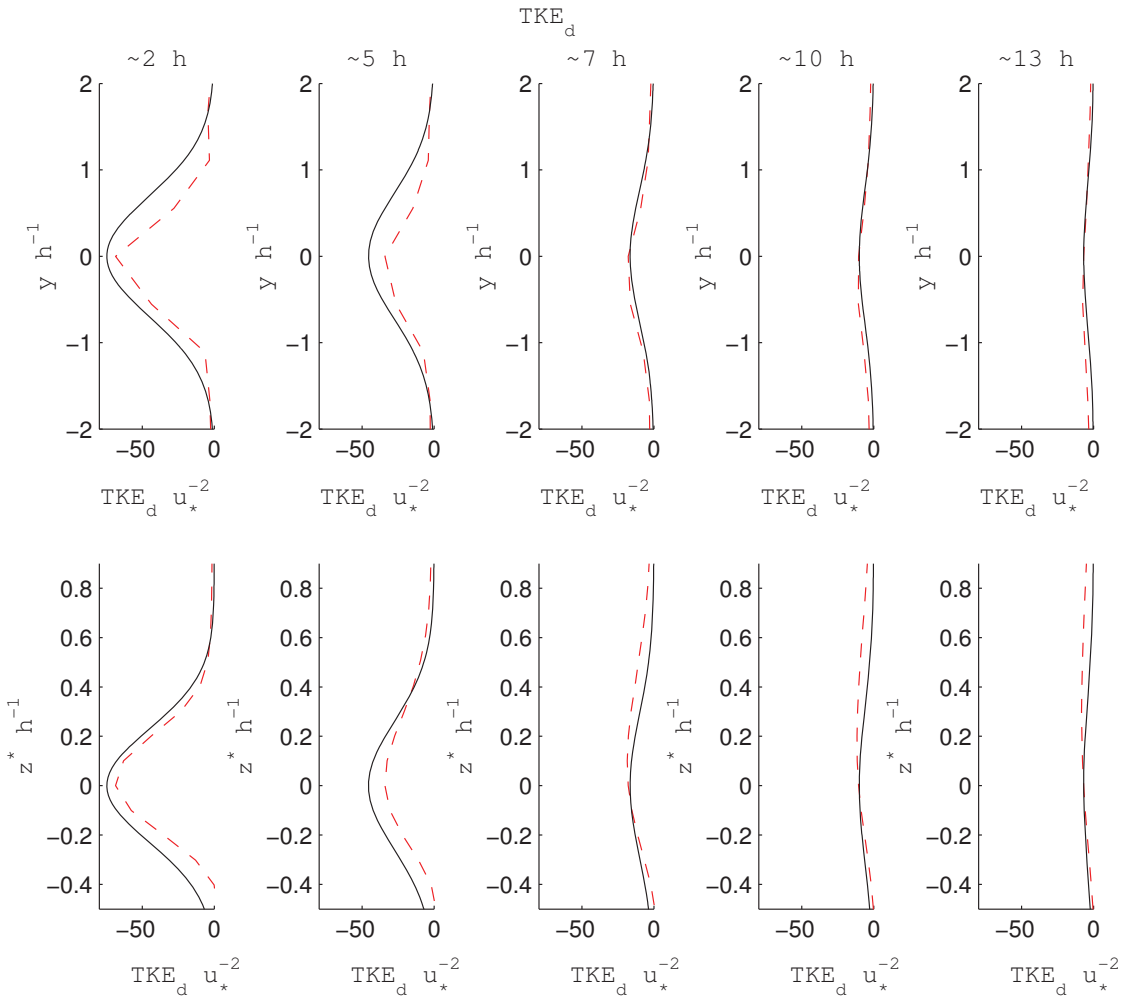

Figure 4.11. TKE defect at several x locations downstream of tree from simulation and from constructed model with $z^* = z - z_m$ and $z_m = 0.7h$. (−−) Simulation, (−) Model.

Quantitatively, in section 4.1 it was found that while the stress follows the same general pattern, the centerline velocity decreases faster than $x^{-2/3}$ and the wake thickness decreases a little slower than $x^{1/3}$ (e.g. Equations (4.4) and (4.1)). Due to these differences between the assumptions required to derive Equation (4.7) and the observed behavior of u_c and δ and the complexity of finding a useful analytical solution that combines equations (4.1), (4.2), (4.4), and (4.1), the following semi empirical relationship for the momentum stress in the wake region behind the tree is used here

$$\overline{u'u'_{rd}} = \frac{r\chi}{\eta}\exp(\frac{-r^2}{\delta^2\lambda^2})$$

where

$$\eta = \left(\sqrt{\frac{\delta^2\lambda^2}{2}}exp(-0.5)\right). \tag{4.8}$$

In equation (4.8) χ is a peak value of defect stress dependent on x, and η is a scaling parameter for χ. χ is found using the same methodology as u_c and κ. The resulting equations for χ are as follows

$$\begin{aligned} \chi/u_*^2 &= -0.53(x/h) + 6.21 \quad \text{if } x/h < 7.77 \\ \chi/u_*^2 &= 6.31(x/h)^{-0.62} \quad \text{if } x/h \geq 7.77. \end{aligned} \tag{4.9}$$

Figure 4.12 depicts spanwise and vertical profiles of the vertical and horizontal stresses respectively using (4.8)-(4.9) and from the LES results. The model is capable of reproducing the LES $u'v'$ in the spanwise direction and $u'w'$ in the vertical direction with moderate accuracy. For the horizontal stress, $u'v'$, the model underpredicts the overall spread of the profile and the peak negative value near the tree. The model is found to overpredict the negative defect stress within the vertical $u'w'$ results near the tree. These deficiencies are seen to improve downstream with the relative error decreasing by around 40 percent over the profiles shown.

In order to test the model's sensitivity to LAD shape the model is tested against the two other tree cases described in section 3.1. For these cases $z_m = 0.3h, 0.5h$ and the maximum LAD values are $L_m = 0.44, 0.5$ respectively. The maximum LAD values were chosen to ensure that the LAI remains around 5 for both cases.

Figure 4.13 shows the velocity defect predicted by the model compared to results from case with $z_m/h = 0.5$. The model is seen to produce comparable accuracy in velocity defect to the $z_m/h = 0.7$ case. The main difference is the presence of a greater flow displacement at the edges of the horizontal profile. The larger displacement could be due to the changes in the LAD profile due to lowering z_m in Equation (3.1).

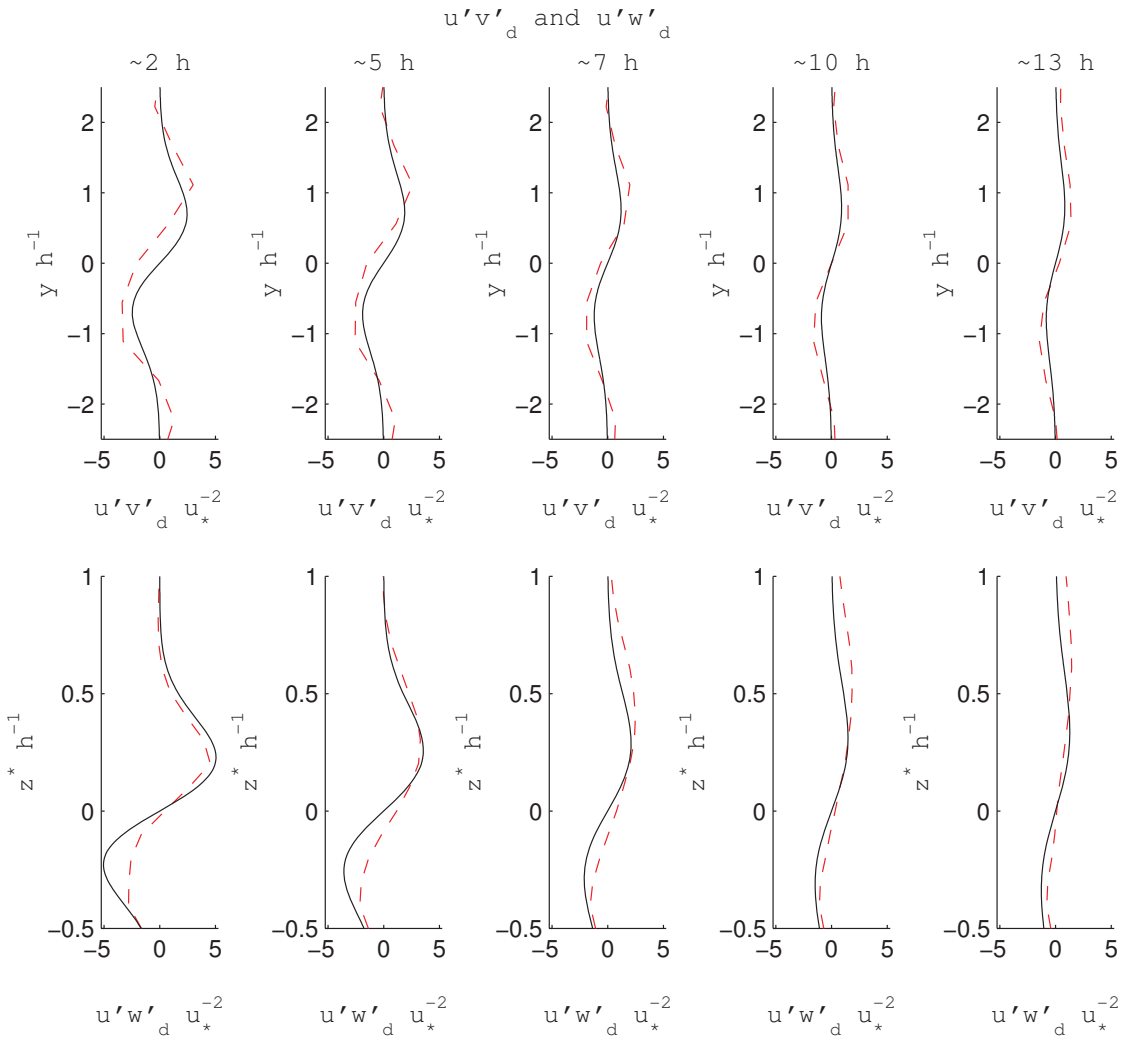

Figure 4.12. Stress defect at several x locations downstream of tree from simulation and from constructed model with $z^* = z - z_m$ and $z_m = 0.7h$. (−−) Simulation, (−) Model.

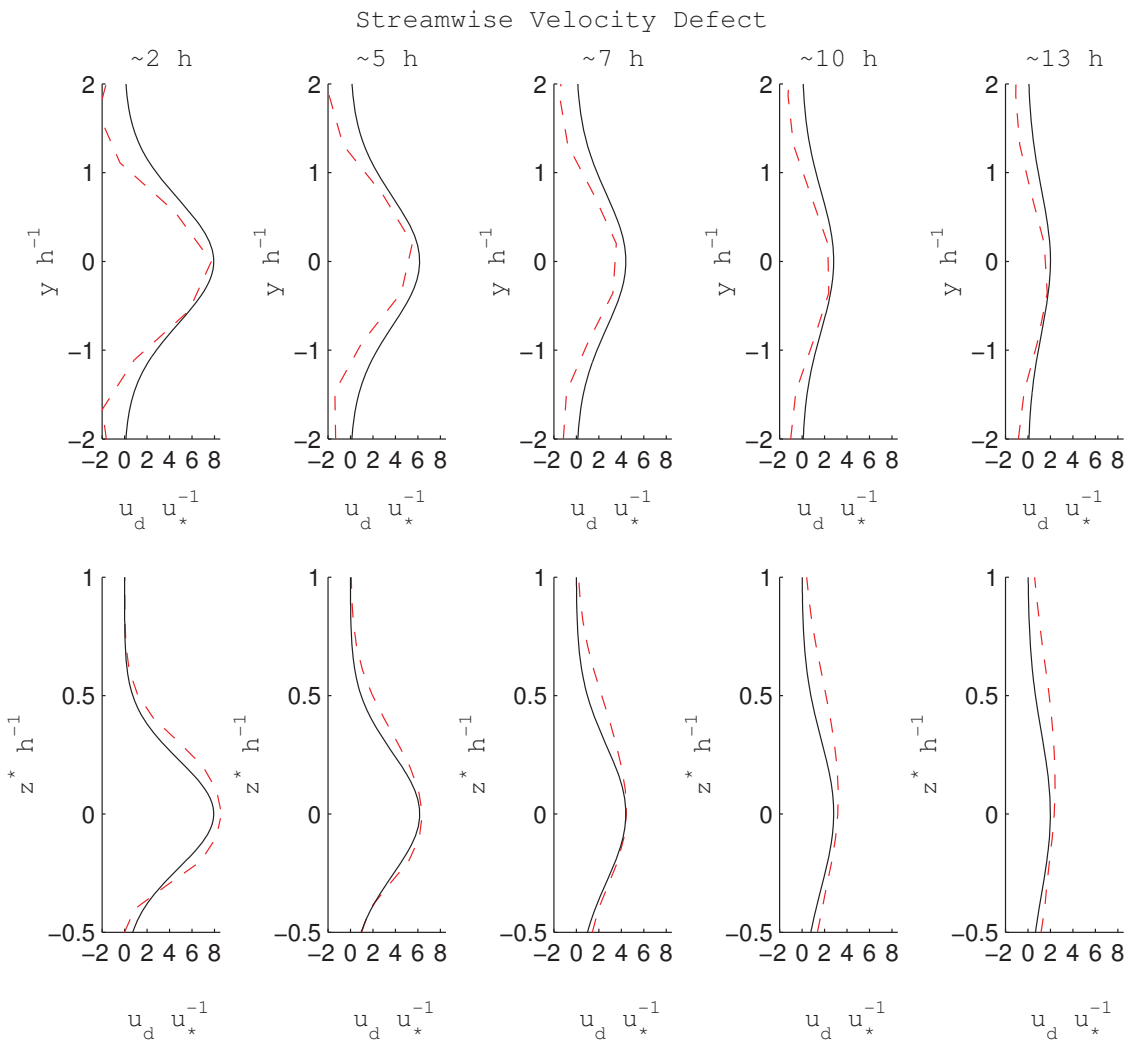

Figure 4.13. Velocity defect at several x locations downstream of tree from simulation and from constructed model with $z^* = z - z_m$ and $z_m = 0.5h$. (−−) Simulation, (−) Model.

Figure 4.14 depicts the TKE defect as predicted by the model and the test case. It is shown that the model overpredicts the peak of TKE near the tree slightly more than the $z_m = 07h$ case. The decrease in peak TKE defect is attributed to the decrease in the maximum LAD value as required to maintain a LAI of 5. The overprediction is seen to improve downstream with it essentially disappearing at around seven tree heights downstream of the tree.

A comparison of the model's predictions against the results from the simulation for turbulent stresses is given in Figure 4.15. It is shown that the accuracy of the model to the simulation is comparable to that of the $z_m/h = 0.7$ case. One difference in the accuracy is a slight overdampening of the peak stress value χ with downstream distance. This is most prevalent in the vertical profile results downstream of the tree. In the vertical results an overprediction of the peak stress values is seen near the tree. The spread of the distribution within the vertical results is underpredicted within the model near the tree. This is seen to improve downstream with essentially no error being found in the spread at around five tree heights downstream of the tree.

The next test case presented is with $z_m/h = 0.3$. It should be noted that such a case is quite unphysical with typical deciduous tree LAD profiles having $z_m/h = 0.5 \rightarrow 0.9$ [6]. The velocity defect results are presented in Figure 4.16. Near the tree it is found that the model overpredicts the maximum velocity defect. This is attributed to the reduction in the maximum LAD value for the tree. The model is seen to incorrectly predict the spread of the vertical profile and vertical location of maximum velocity defect near the tree. These could be due to interference with the ground or due to the alterations to the LAD profile as previously discussed.

The results for TKE defect are presented in Figure 4.17. As can be seen the model greatly overpredicts the maximum TKE defect near the tree similar to the $z_m/h = 0.5$ results. This great overprediction is attributed, like the $z_m/h = 0.5$ case, to the reduction in maximum LAD value. The overprediction is found to essentially disappear at around seven tree heights away from the tree. In the vertical profiles the model is found to incorrectly predict the centerline of the distribution. This same defect was seen in the velocity defect for the case and is attributed to the same reasons.

The stress defect from the model and from the test case is presented in Figure 4.18. The model is shown to capable of reproducing the horizontal stress profile with similar accuracy to the $z_m/h = 0.5$ case. Within the vertical profiles it is seen that the model incorrectly predicts the vertical location of maximum stress near the tree.

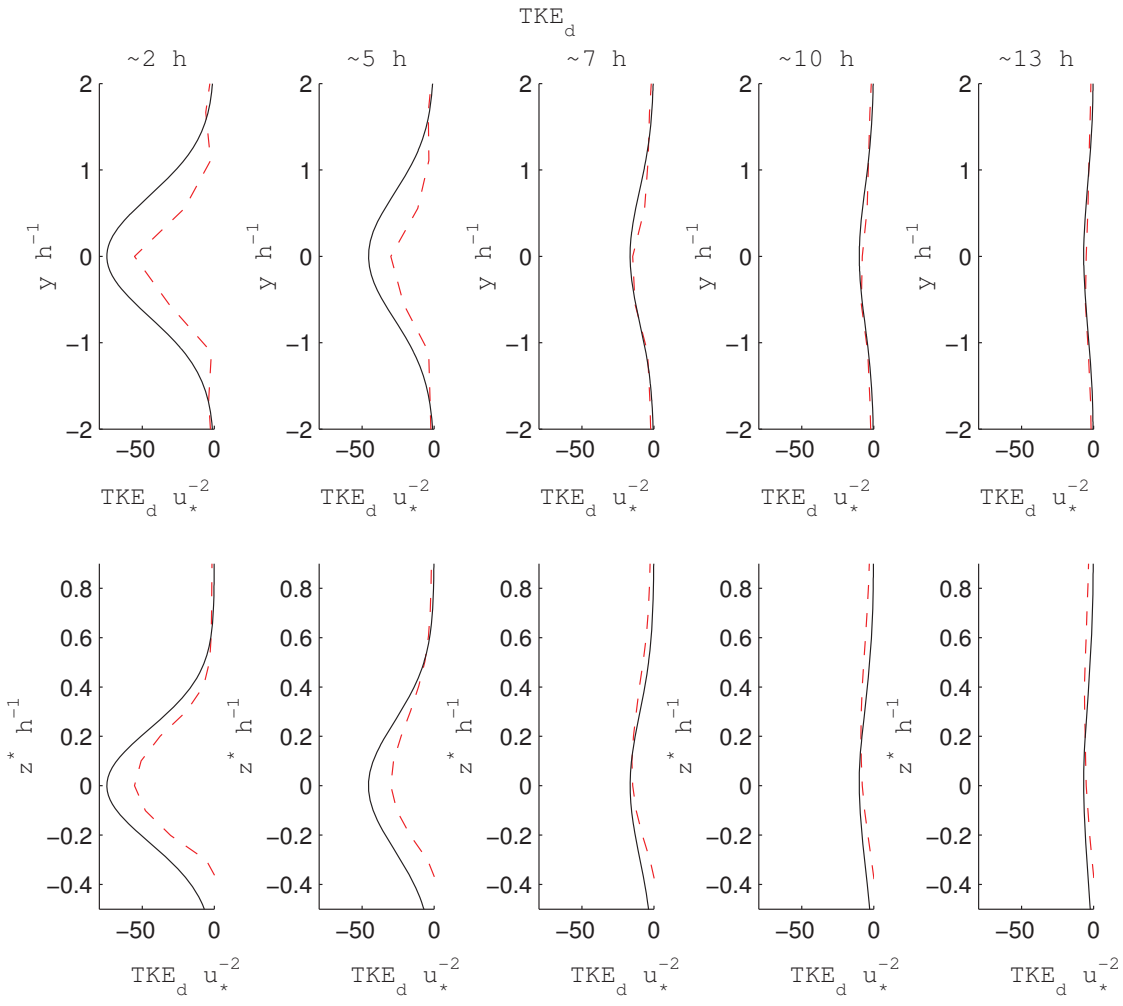

Figure 4.14. TKE defect at several x locations downstream of tree from simulation and from constructed model with $z^* = z - z_m$ and $z_m = 0.5h$. (−−) Simulation, (−) Model.

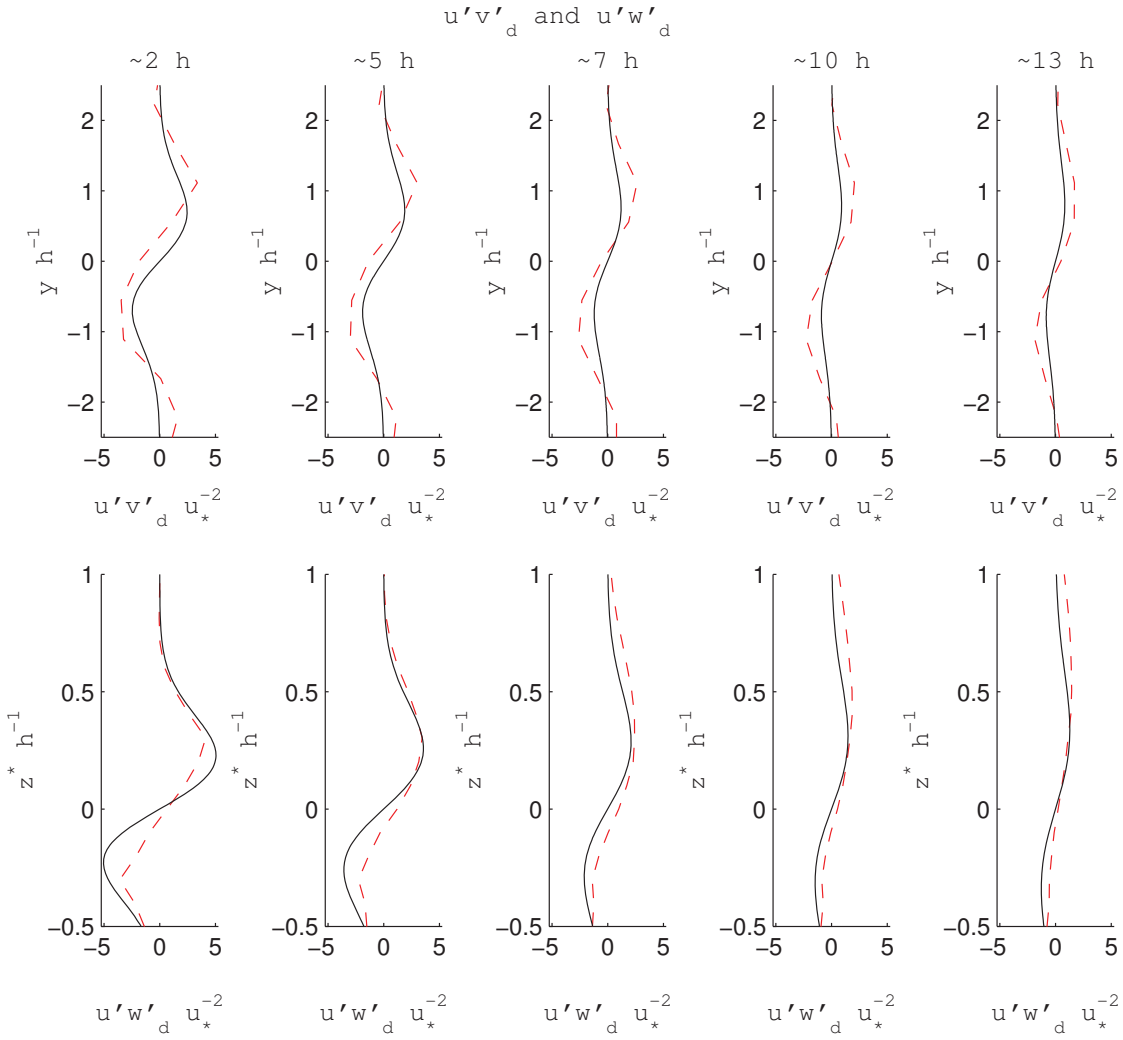

Figure 4.15. Stress defect at several x locations downstream of tree from simulation and from constructed model with $z^* = z - z_m$ and $z_m = 0.5h$. (−−) Simulation, (−) Model.

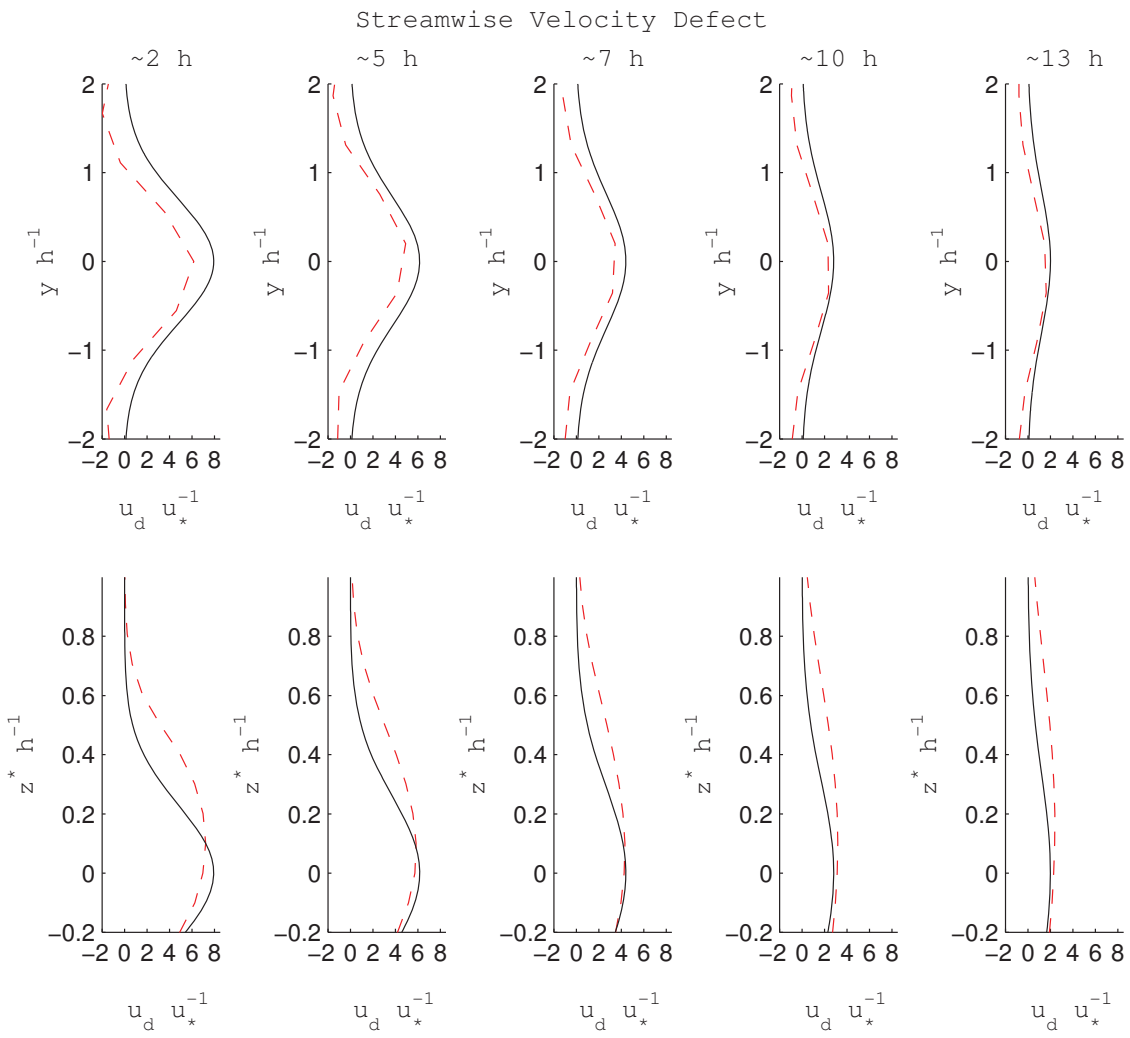

Figure 4.16. Velocity defect at several x locations downstream of tree from simulation and from constructed model with $z^* = z - z_m$ and $z_m = 0.3h$. (−−) Simulation, (−) Model.

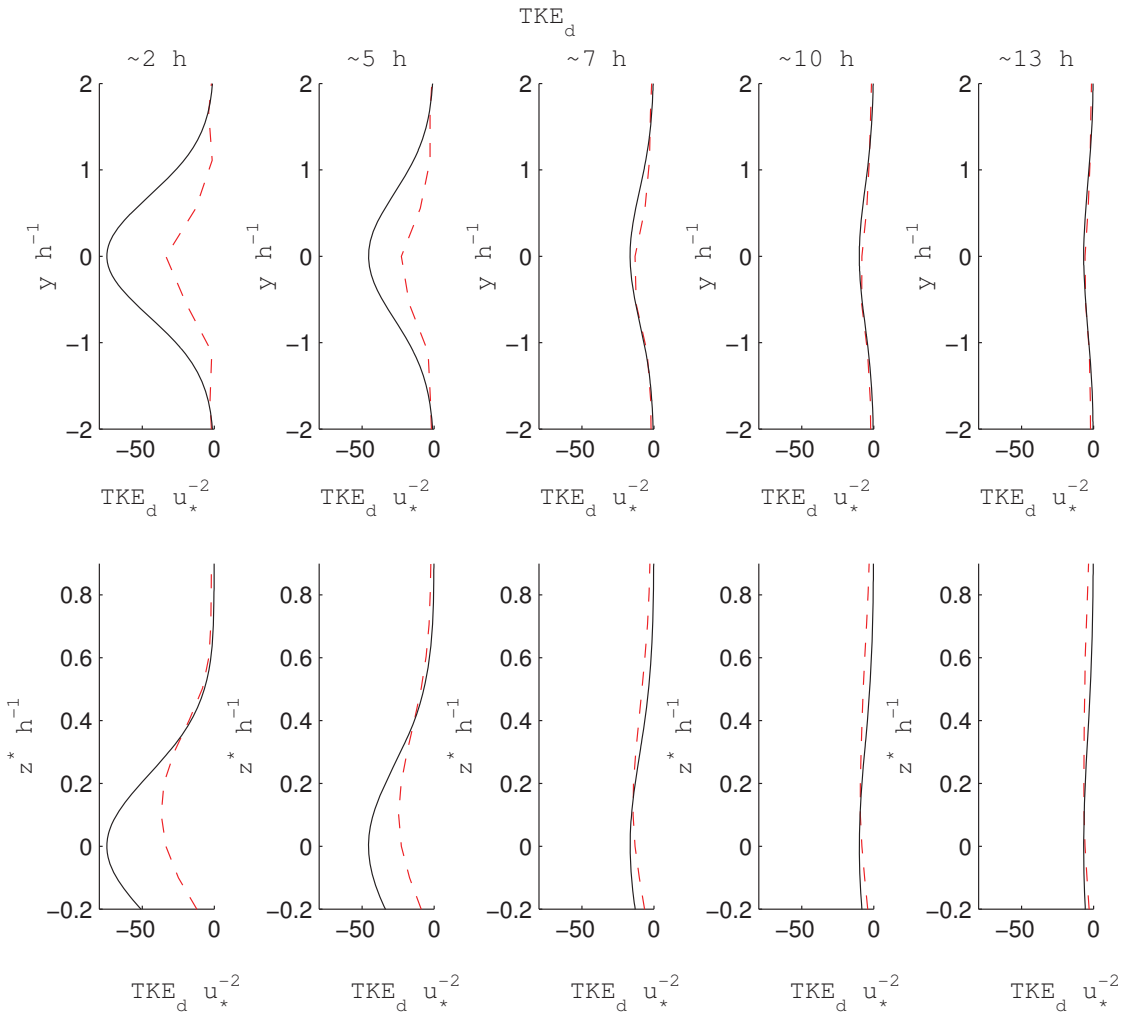

Figure 4.17. TKE defect at several x locations downstream of tree from simulation and from constructed model with $z^* = z - z_m$ and $z_m = 0.3h$. (−−) Simulation, (−) Model.

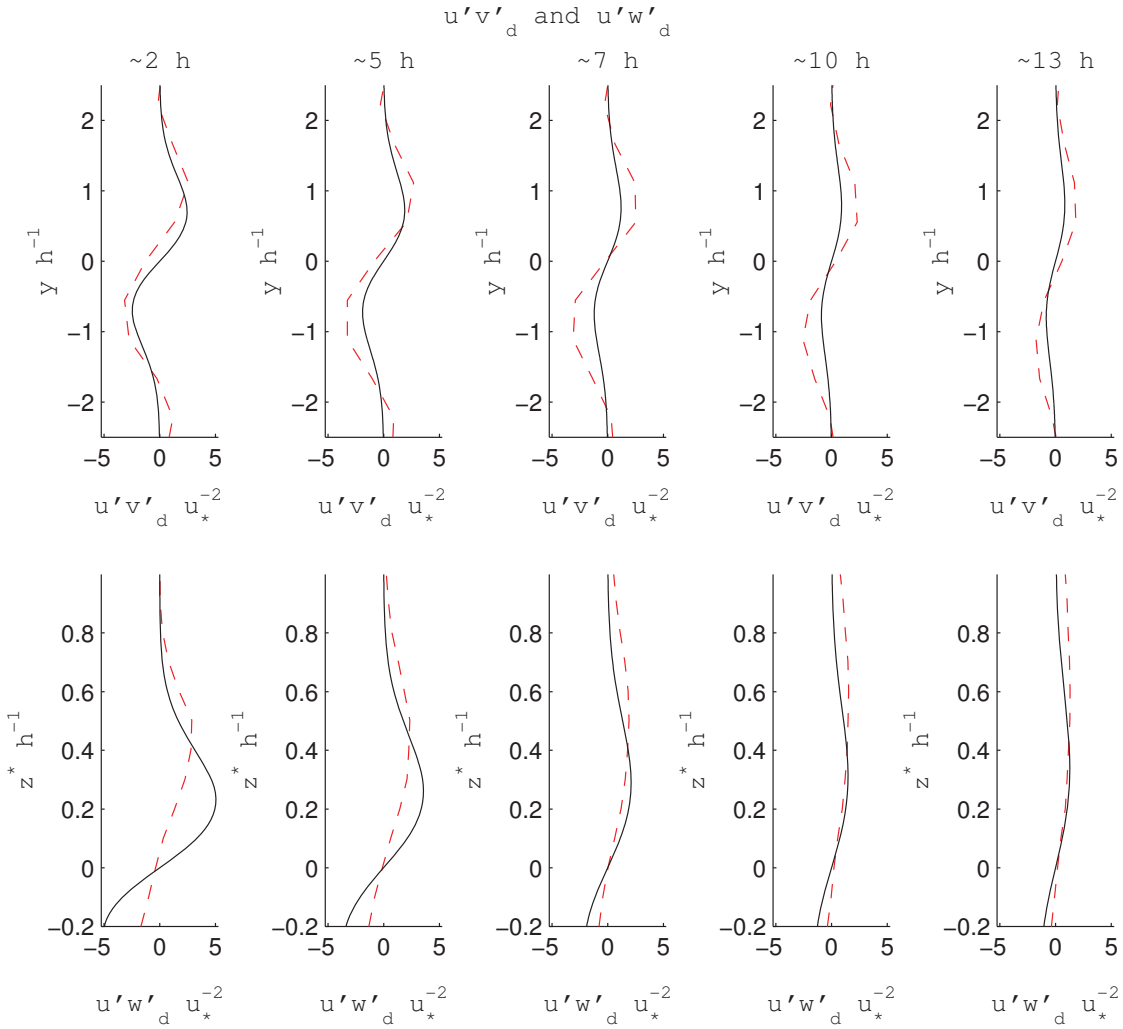

Figure 4.18. Stress defect at several x locations downstream of tree from simulation and from constructed model with $z^* = z - z_m$ and $z_m = 0.3h$. (−−) Simulation, (−) Model.

CHAPTER 5

CONCLUSION

A large-eddy simulation study was conducted to characterize the bulk momentum and turbulence features of flow around an isolated deciduous tree in the atmospheric boundary layer under neutral conditions. In addition to characterizing the flow field, a simplified model that contained the essential features of flow around an isolated tree was constructed. Within the results a section of high streamwise velocity defect and turbulent kinetic energy is found behind the tree with accelerated flow around the edges of the crown. This region began near the region of maximum leaf area density and spread outwards downstream. The spanwise and vertical velocity was found to entrain freestream fluid inwards towards the wake, fueling the increase in wake size. The region of turbulent kinetic energy was found to be dominated by the streamwise velocity variance. A peak in turbulent stress was found near the top and bottom of the crown of the tree with a transition occurring near the location of maximum leaf area density. These basic structures of turbulent stress, velocity defect and spanwise/vertical velocity are similar to results for axisymmetric and plane wakes. These similarities were used as a motivation for the creation of a simplified empirical model.

The empirical model was created through a series of data fits of simulation results to parameters of wake spread, velocity decay, TKE decay, and stress decay. Two major differences were incorporated into the empirical model from that of canonical plane or axisymmetric wake results. First, it was found that the wake region of the tree was non-symmetric being wider than it was tall. This was addressed by adding an angular dependence in the wake spread parameterization. The second major difference between the model and plane or axisymmetric results was the addressing of different flow regimes. Typically in plane wake or axisymmetric wake results only the far wake region is considered [9]. It was desired for the model to incorporate both the near wake and far wake regimes. It was found that the various parameters could be fit with reasonable accuracy to a linear fit in the near wake region and to a general power law in the far wake region.

The model was tested for accuracy with changed leaf area density profile shape. The modification tested was the adjustment of the vertical location of maximum vertical leaf area density and maximum leaf area density value. It was found that when this location was adjusted to lower locations the peak turbulent kinetic energy and velocity defect was overpredicted by the model. This issue was seen to resolve with distance downstream and was only present in the near wake region. This issue was attributed to the decrease in maximum LAD value at these lower cases. In the lowest case tested it was seen that the model was incapable of predicting the correct vertical location of maximum velocity defect, TKE, and vertical turbulent stress. This was attributed to both changes in the LAD profile and also to the influence of the ground. The lowest case tested was an unphysical case for a deciduous tree with a maximum LAD location of $z_m/h = 0.3$. Given this, the failings of the model for this case are considered negligible given that the model should not realistically be used on such a case. Overall, the model created was found to accurately reproduce the turbulent stresses, the streamwise velocity defect, and the turbulent kinetic energy in the near and far wake regions for deciduous trees.

REFERENCES

[1] A. Agrawal and A. K. Prasad, *Integral solution for the mean flow profiles of turbulent jets, plumes, and wakes*, J. of Fluids Engin. **125** (2003), 813–822.

[2] K. Bai, C. Meneveau, and J. Katz, *Near-wake turbulent flow structure and mixing length downstream of a fractal tree*, Boundary-Layer Meteorol. **143** (2012), 285–308.

[3] B. N. Bailey and R. Stoll, *Turbulence in sparse, organized vegetative canopies : A large-eddy simulation study*, Boundary-Layer Meteorol. (2012).

[4] D.D. Baldocchi and T.P. Meyers, *Turbulence structure in a deciduous forest*, Boundary-Layer Meteorol **43** (1987), 345–364.

[5] G. Bohrer, G. G. Katul, R. Nathan, R. L. Walko, and R. Avissar, *Exploring the effects of microscale structural heterogeneity of forest canopies using large-eddy simulation*, Boundary-Layer Meteorol. **132** (2009), 351–382.

[6] L. Branislava and D. T. Mihailovic, *An empirical relation describing leaf-area density inside the forest for environmental modeling*, Journ. of Appl. Meteorol **43** (2004), 641–645.

[7] F. Bruchert, O. Speck, and H.C. Spatz, *Oscillations of plants' stems and their damping: theory and experimentation*, Philos. Trans. R. Soc **358** (2003), 1487–1492.

[8] D. Cava and G.G. Katul, *Spectral short-circuiting and wake production within the canopy trunk space of an alpine hardwood forest*, Boundary-Layer Meteorol **126** (2008), 415–431.

[9] P.A. Davidson, *Turbulence an introduction for scientists and engineers*, Cambridge University Press, 2004.

[10] E. de Langre, *Effects of wind on plants*, Annu. Rev. Fluid Mech. **40** (2008), 141–168.

[11] United Nations. Population Division, *World urbanization prospects : the 2009 revision*, United Nations, 2010.

[12] S. Dupont and Y. Brunet, *Influence of foliar density profile on canopy flow: A large-eddy simulation study*, Agric. Meteorolol **148** (2008), 976–990.

[13] M.J. Dwyer, E.G. Patton, and R.H. Shaw, *Turbulent kinetic energy budgets from a large-eddy simulation of airflow above and within a forest canopy*, Boundary-Layer Meteorol **84** (1997), 23–43.

[14] J. Finnigan, *Turbulence in plant canopies*, Annu. Rev. Fluid Mech. **32** (2000), 519–571.

[15] J. J. Finnigan and R. H. Shaw, *Double-averaging methodology and its application to turbulent flow in and above vegetation canopies*, Acta Geophys **5** (2008), 534–561.

[16] M. Garcia-Villalba and J. Fŕohlich, *Les of a free annular swirling jet - dependence of coherent structures on pilot jet and the level of swirl*, Int. J. Heat Fluid Flow **27** (2006), 911–923.

[17] E.F. Gilman and D.G. Watson, *Acer rubrum : Red maple*, Tech. report, University of Florida. IFAS, 2006.

[18] G. Gross, *A numerical study of air flow within and around a single tree*, Boundary-Layer Meteorol. **40** (1987), 311–327.

[19] C. Ho and P. Huerre, *Perturbed free shear layers*, Annu. Rev. Fluid Mech. **16** (1984), 365–422.

[20] J. Huang, M. Cassiani, and J.D. Albertson, *The effects of vegetation density on coherent turbulent structures within the canopy sublayer: A large-eddy simulation study*, Boundary-Layer Meteorol **133** (2009), 253–275.

[21] M.R. Irvine, B. A. Gardiner, and M.K. Hill, *The evolution of turbulence across a forest edge*, Boundary-Layer Meteorol **84** (1997), 467–496.

[22] M.J. Judd, M. R. Raupach, and J.J. Finnigan, *A wind tunnel study of turbulent flow around single and multiple windbreaks, part i: Velocity fields*, Boundary-Layer Meteorol **80** (1996), 127–165.

[23] H. Mayer, *Wind-induced tree sways*, Trees Struct. Funct. **1** (1987), 195–206.

[24] J. Moore and D. Maguire, *Natural sway frequencies and damping ratios of trees: concepts, review and synthesis of previous studies*, Trees Struct. Funct **18** (2004), 195–203.

[25] M.D. Novak, J.S. Warland, A.L Orchansky, R. Ketler, and S. Green, *Wind tunnel and field measurements of turbulent flow in forests. part i: Uniformly thinned stands*, Boundary-Layer Meteorol **95** (2000), 457–495.

[26] S.A. Orszag and Y.H. Pao, *Numerical computation of turbulent shear flows*, Adv. Geophys **18A** (1974), 224–236.

[27] E. G. Patton, R. H. Shaw, M. J. Judd, and M. R. Raupach, *Large-eddy simulation of windbreak flow*, Boundary-Layer Meteorol **87** (1998), 275–306.

[28] D. Poggi and G.G. Katul, *The effect of canopy roughness density on constitutive components of the dispersive stresses.*, Exp. Fluids **45** (2008), 111–121.

[29] D. Poggi, A. Porporato, L. Ridolfi, J.D. Albertson, and G.G. Katul, *The effect of vegetation density on canopy sub-layer turbulence*, Boundary-Layer Meteorol **111** (2004a), 565–587.

[30] S. B. Pope, *Turbulent flows*, Cambridge University Press, 2000.

[31] F. Porté-Agel, Y-T. Wu, H. Lu, and R. J. Conzemius, *Large-eddy simulation of atmospheric boundary layer flow through wind turbines and wind farms*, Journ. of Wind Engin. and Indust. Aerodyn **99** (2011), 154–168.

[32] C. Py, E. de Langre, and B. Moulia, *A frequency lock-in mechanism in the interaction between wind and crop canopies*, J. Fluid Mech. **568** (2006), 425–449.

[33] M.R. Raupach, J.J. Finnigan, and Y. Brunet, *Coherent eddies and turbulence in vegetation canopies: The mixing-layer analogy*, Boundary-Layer Meteorol **78** (1996), 351–382.

[34] A. Roshko, *Experiments of the flow past a circular cylinder at very high reynolds number*, Jour. of Fluid Mech **10** (1961), 345–356.

[35] R.J. Scholes and S.R. Archer, *Tree-grass interactions in savannas*, Annu. Rev. Ecolog. Syst **28** (1997), 517–544.

[36] R. H. Shaw and U. Schumann, *Large-eddy simulation of turbulent flow above and within a forest*, Boundary-Layer Meteorol **61** (1992), 47–64.

[37] R. Stoll and F. Porté-Agel, *Dynamic subgrid-scale models for momentum and scalar fluxes in large-edy simulations of neutrally stratified atmospheric boundary layers over heterogeneous terrain*, Water Resources Res. **42** (2006), W01,409.

[38] _____, *Surface heterogeneity effects on regional-scale fluxes in stable boundary layer: Surface temperature transitions*, J. Atmos. Sci **66** (2009), 412–431.

[39] H-B. Su, R.H. Shaw, K.T.P. U, C-H. Moeng, and P.P. Sullivan, *Turbulent statistics of neutrally stratified flow within and above a sparse forest from large-eddy simulation and field observations*, Boundary-Layer Meteorol **88** (1998), 363–397.

[40] H.B. Su, R.H. Shaw, U. K.T. Paw, C.H. Moeng, and P.P. Sullivan, *Turbulent statistics of neutrally stratified flow within and above a sparse forest from large-eddy simulation and field observations*, Agric. Meteorol **148** (2008), 862–882.

[41] G.R. Tabor and M.H. Baba-Ahmadi, *Inlet conditions for large eddy simulation: a review*, Comp. and Fluids **39** (2010), 553–567.

[42] E.S. Takle, H. Wang, R.A. Schmidt, J.R. Brandle, I.V. Livina, and R.L. Jairell, *Pressure perturbations around shelterbelts: Measurements and model results*, Symp. Boundary Layers turbul, 12th, Vancouver,, 1997, pp. 563–564.

[43] Y.H. Tseng, C. Meneveau, and M.B. Parlange, *Modeling flow around bluff bodies and predicting urban dispersion using large eddy simulation*, Environ. Sci. Technol. **40** (2006), 2653–2662.

[44] F. Wan and F. Porté-Agel, *Large-eddy simulation of stably-stratified flow over a steep hill*, Boundary-Layer Meteorol **138** (2011), 367–384.

[45] F. Wan, F. Porté-Agel, and R. Stoll, *Evaluation of dynamic subgrid-scale models in large-eddy simulation of neutral turbulent flow over a two-dimensional sinusoidal hill*, Atmosph. Environ. **41** (2007), 27192728.

[46] H. Wang and E.S. Takle, *A numerical simulation of boundary-layer flows near shelterbelts*, Boundary-Layer Meteorolo **75** (1995), 141–173.

[47] _____, *Inumerical simulation of shelterbelt effects on wind direction*, J. Appl. Meteorol **34** (1996), 2206–2219.

[48] H. Wang, E.S. Takle, and J. Shen, *Shelterbelts and windbreaks: mathematical modeling and computer simulations of turbulent flows*, Annu. Rev. Fluid Mech **33** (2001), 549–586.

[49] P. Wang, X. S. Bai, M. Wessman, and J. Klingmann, *Large eddy simulation and experimental studies of a confined turbulent swirling flow*, Phys. Fluids **16** (2004), 3306–3324.

[50] T. Watanabe, *Large-eddy simulation of coherent turbulence structures associated with scalar ramps over plant canopies*, Boundary-Layer Meteorol **112** (2004), 307–341.

[51] C. Yi, *Momentum transfer within canopies*, J. Appl. Meteorol. Climatol. **47** (2007), 262–275.

[52] W. Yue, M. B. Parlange, C. Meneveau, W. Zhu, R. van Hout, and J. Katz, *Large-eddy simulation of plant canopy flows using plant-scale representation*, Boundary-Layer Meteorol **124** (2007), 183–203.